Supplementary Information

Covalently interconnected transition metal dichalcogenide networks *via* defect engineering for high-performance electronic devices

Stefano Ippolito[a], Adam G. Kelly[b], Rafael Furlan de Oliveira[a], Marc-Antoine Stoeckel[a], Daniel Iglesias[a], Ahin Roy[c], Clive Downing[c], Zan Bian[d], Lucia Lombardi[d], Yarjan Abdul Samad[d], Valeria Nicolosi[c], Andrea C. Ferrari[d], Jonathan N. Coleman[b], Paolo Samorì[a,*]

* Corresponding author: samori@unistra.fr

Table of Contents

1. Raw materials and characterization techniques……...S2
2. Production and characterization of solution-processed MS_2……..S4
3. Morphological and structural investigations……..S8
4. X-ray photoelectron spectroscopy (XPS) analysis……....S10
5. Raman spectroscopy analysis……..S14
6. Multiscale characterization of functionalized MoS_2 films……..S16
7. Electrical properties of thin-film transistors……S22
8. Temperature-dependent electrical characteristics……....S28
9. Ex-situ functionalization……S32
10. References…….....S35

1. Raw materials and characterization techniques

MoS_2 and WS_2 powders (purity ≥99%) are sourced from Sigma Aldrich and used as provided. ReS_2 crystals (purity ≥99.995%) from HQ Graphene are used as provided. Benzene-1,4-dithiol (BDT), Thiophenol (TP), Propane-1,3-dithiol (PDT) and Benzene-1,4-diamine (PPD) with purity ≥99% are purchased from Sigma Aldrich. All chemicals are used without further purification steps.

Spectroscopic characterizations

- UV-Vis absorption spectra are recorded on a JASCO v670 spectrometer using quartz cuvettes (light path = 10 mm) under ambient conditions.
- Raman spectra are recorded under ambient conditions with a Renishaw inVia spectrometer at 532 nm with a 100x objective (numerical aperture 0.85). The power is kept below 1 mW to avoid local heating and damage effects.
- X-ray photoelectron spectroscopy (XPS) is performed with a Thermo Scientific K-Alpha X-ray photoelectron spectrometer, operating with a base chamber pressure of ~ 10^{-9} mbar and an Al anode as X-ray source ($Al_{K\alpha}$ radiation of 1486.6 eV). The X-ray beam spot size is ~ 400 μm. Peak fitting is performed with constrains on the full width half maximum (FWHM) and the peak area ratio of the spin-orbit components.
- Photo-Electron Spectroscopy in Air (PESA) analysis is performed with a Riken Keiki AC-2 photoelectron spectrometer under ambient conditions.
- Nuclear magnetic resonance (NMR) analysis is performed with a Bruker Avance III HD 400 MHz, using cyclohexane-d_{12} as solvent. The MestreNova software was used to process the data.

Morphological, structural and surface characterizations

- Scanning electron microscopy (SEM) is performed with a Quanta FEG 450, operating with a chamber pressure ~10^{-6} torr and gun pressure ~10^{-9} torr, working at 20-30 kV.
- High-angle annular dark-field (HAADF) aberration-corrected scanning transmission electron microscopy (AC-STEM) is carried out in a NION UltraSTEM200, operating at 60 kV. The probe convergence semi-angle is 35 mrad, with a probe diameter of 1.2 Å. The inner and outer collection angles of the HAADF detector are 85 and 185 mrad, respectively.

- X-ray diffraction (XRD) experiments are performed with a Rigaku Smartlab equipped with a rotating anode of $Cu_{K\alpha}$ radiation operating at 45 kV and 300 mA.
- Atomic force microscopy (AFM) is done with a Bruker Dimension Icon microscope in ambient conditions, operating in tapping mode and using TESPA-V2 tips with spring constant k = 42 N/m.
- The film thickness is measured with a KLA-Tencor Alpha-Step IQ profilometer operating in ambient conditions.
- Optical microscopy imaging is performed with a Olympus BX51 microscope operating under ambient conditions.
- Static water contact angle measurements are performed with a Krüss DSA 100 instrument, operating under ambient conditions.
- Dynamic light scattering (DLS) and Zeta-Potential measurements are performed with a Beckman Coulter "Delsa Nano Submicron Particle Size and Zeta Potential" instrument, in ambient conditions.
- Mechanical tests are performed with digital force gauge "Mark-10, M7-025E, 1N" coupled with the motorized test stand "Mark-10, ESM-303E", operating under ambient conditions.

Electrical characterizations

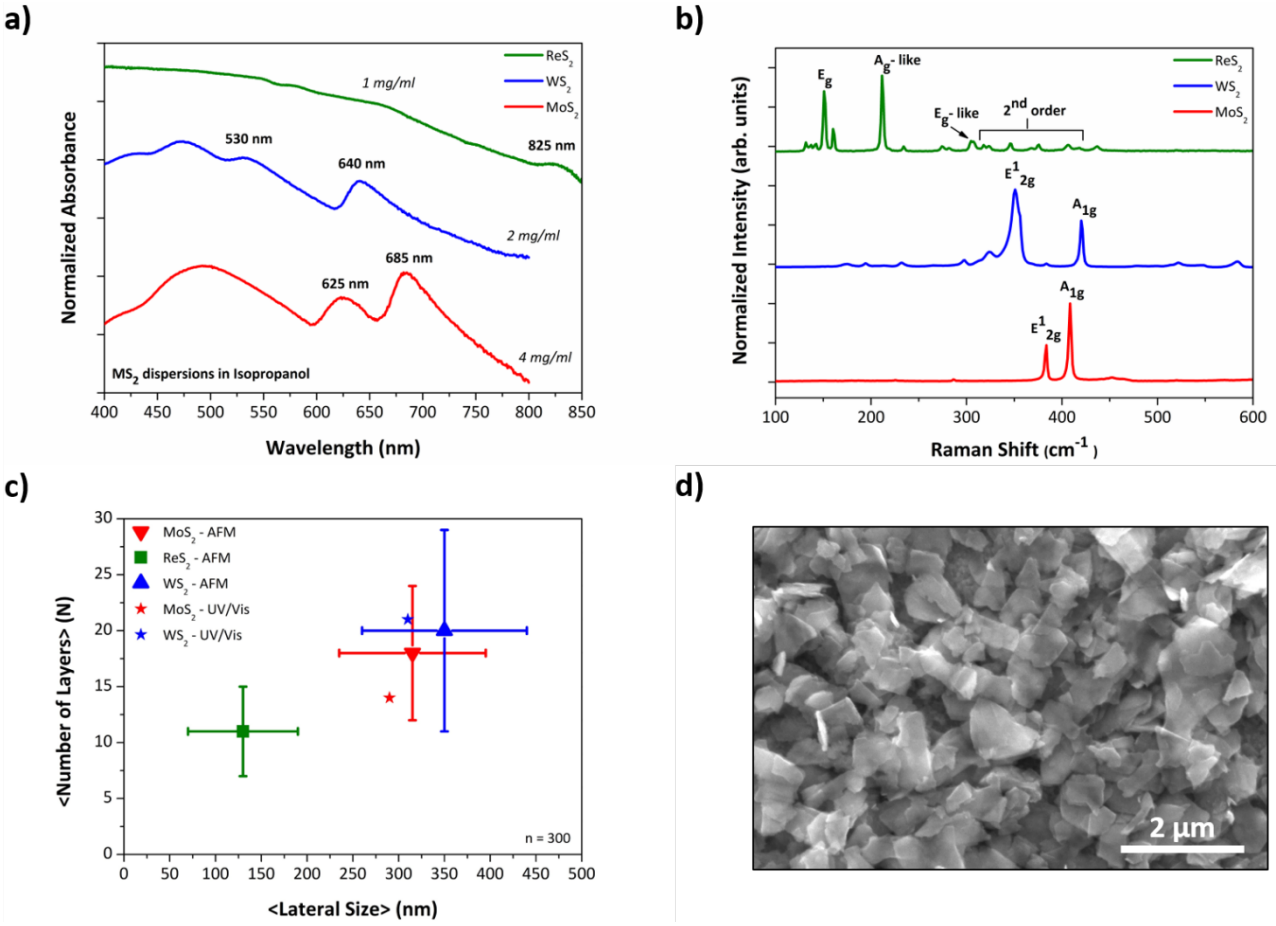
- The electrical properties of liquid-gated thin-film transistors (LG-TFTs) were investigated under N_2 atmosphere (inside glovebox) using a PM5 Cascade Microtech probe station connected with a Keithley 2636A SourceMeter.
- Cyclic voltammetry (CV) experiments are performed using a CH Instruments 600E Series Electrochemical Analyzer/Workstation, under ambient conditions. A three-electrode cell set-up is used with an Ag/AgCl reference electrode and a Pt counter electrode.
- Temperature-dependent electrical characterizations is carried out using an Oxford Instruments Optistat DN-V cryostat, operating in the range 80-300 K (liquid N_2) coupled with a Keithley 2636 SourceMeter unit.

2. Production and characterization of solution-processed MS_2

MoS_2 and WS_2 inks are obtained by sonicating the respective powders in N-Methyl-2-pyrrolidone (NMP). An initial concentration of 20 mg/ml is processed for 1h in 80 ml of NMP using a horn tip sonicator (Sonics Vibra-cell VCX-750 ultrasonic processor) at 60% amplitude. The dispersion is then centrifuged at 3218 g for 1h using a Hettich Mickro 220R, after which the supernatant is discarded to remove potential contaminants from the starting powder. The sediment is then redispersed in fresh NMP and sonicated under the same conditions for 6h. This process gives a polydisperse stock dispersion from which flakes can be size-selected by centrifugation. For each material, the polydisperse stock is first centrifuged at 106.4 g for 90 min to remove the largest aggregates, with the sediment retained for future exfoliation. The supernatant is then centrifuged at 425 g for 90 min to separate the smaller flakes. This sediment is then redispersed in 30 ml of isopropanol (IPA).

ReS_2 inks are prepared by mixing the starting powders into IPA (Aldrich Sigma, >99.5%), and exfoliating for 3h by using a bath sonication (Fisherbrand). The exfoliated dispersion is left to rest for 3 days to allow unexfoliated flakes to settle down by gravity. The supernatant is then collected for ink formulation. This is re-dispersed into IPA and re-exfoliated in a bath sonicator for 3h, collecting the supernatant again. The process is then repeated. All collected supernatants are mixed and sonicated for 1h to formulate the ReS_2 ink. This is then placed into a vacuum oven at 40^{o}C for 3h to evaporate IPA and increase the concentration.

Upon production, the solution-processed MS_2 material inks (M = Mo, W, Re) are characterized to assess their concentration, quality and purity. The results are reported in Supplementary Fig. 1.



Supplementary Fig. 1 | Spectroscopic and morphological characterization of solution-processed MS_2. **a**, UV-Vis spectra (solution). **b**, Raman spectra (film). **c**, Statistical AFM analysis performed on individual MS_2 flakes (300, overall) and comparison with values estimated *via* UV-Vis spectroscopy. **d**, Typical SEM image of drop-cast MoS_2 flakes.

UV-Vis spectroscopy is used to estimate the concentration of the three MS_2 dispersions. This gives ~4, 2 and 1 mg/ml for MoS_2, WS_2 and ReS_2, respectively[1]. The morphological features obtained by AFM imaging are compared to those obtained *via* spectroscopic investigation for MoS_2 and WS_2 flakes, the latter estimated by UV-Vis as for References 2 and 3. The average lateral size and thickness estimated by UV-Vis match the AFM analysis (Supplementary Table 1).

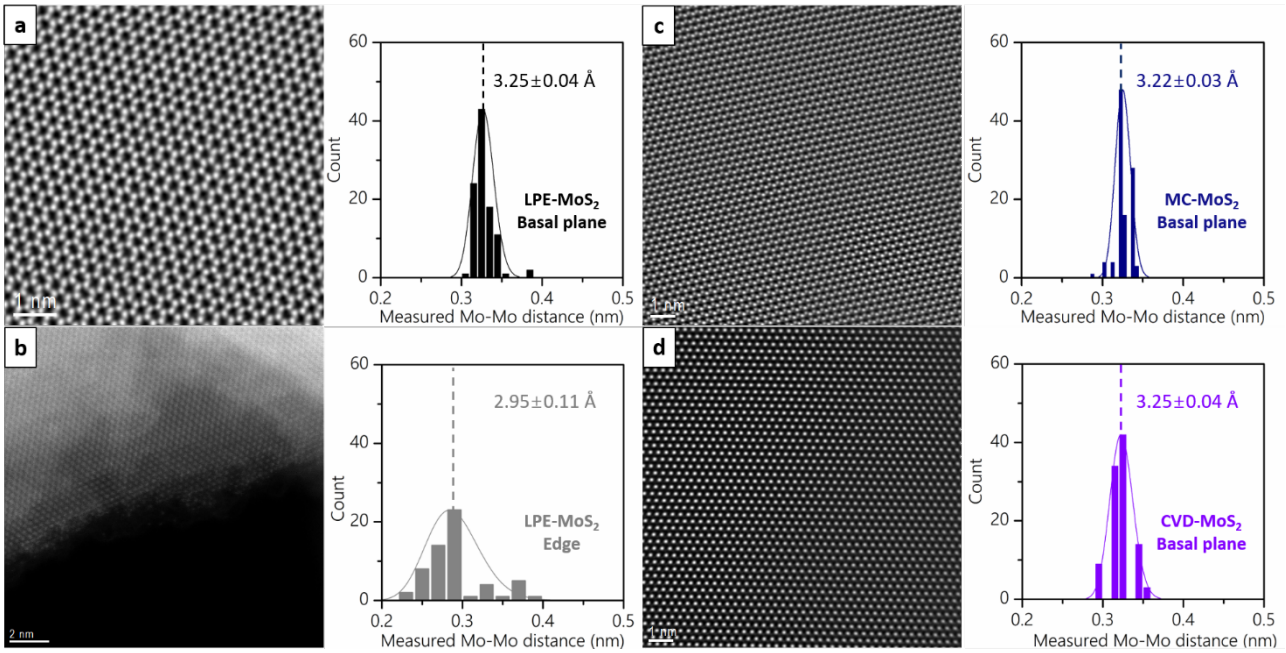
TMD	<N> AFM	<L> AFM	<N> UV-Vis	<L> UV-Vis	Ref.
MoS_2	18 ± 6	315 ± 80 nm	14	290 nm	2
WS_2	20 ± 9	350 ± 90 nm	21	310 nm	3
ReS_2	11 ± 4	130 ± 60 nm	-	-	-

Supplementary Table 1: Morphological features of individual solution-processed MS_2 flakes and comparison between UV-Vis and AFM analysis. <N> = average number of layers, <L> = average lateral size.

The UV-Vis spectra in Supplementary Fig. 1a show the characteristic excitonic transitions for the three MS_2. In MoS_2 and WS_2 the peaks arise from direct-gap transitions at the K point of the Brillouin zone, resulting in absorption bands at 625 and 685 nm for MoS_2, and at 530 and 640 nm for WS_2 flakes[4]. Similarly, the ReS_2 spectrum shows an absorption band at ~825 nm corresponding to the direct-gap transition[5].

The Supplementary Fig. 1b plots typical Raman spectra for the three MS_2. In-plane E_g modes and out-of-plane A_g modes are highlighted, corresponding to two main peaks located at 384 cm^{-1} and 405 cm^{-1} for MoS_2, 352 cm^{-1} and 420 cm^{-1} for WS_2, 154 cm^{-1} and 218 cm^{-1} for ReS_2[5,6].

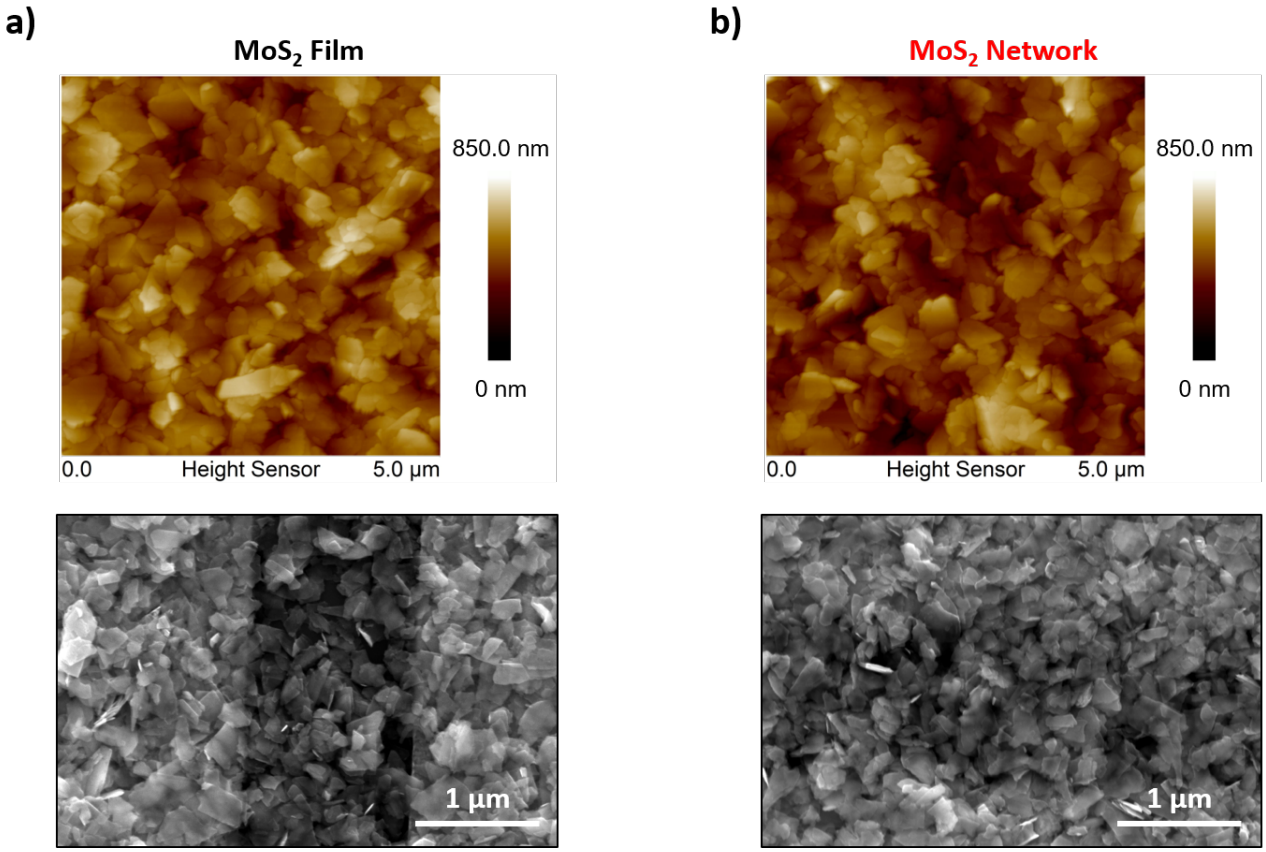
In order to corroborate our claim about the higher defect density at the edges in solution-processed TMDs with respect to basal planes, we performed a meticulous high-angle annular dark-field scanning transmission electron microscopy (HAADF-STEM) investigation. We measured the Mo-Mo distance for MoS_2 prepared by LPE, mechanical cleavage (MC) and chemical vapour deposition (CVD), as the amount and kind of defects depend on the synthesis/production method[7]. As shown in Supplementary Fig. 2, the Mo-Mo distance in the basal plane is similar for all samples. At the edges of LPE-MoS_2 the Mo-Mo distance shortens by ~30 pm with respect to that on the basal plane. Such an effect is due to a higher defect density that can originate because of V_S mainly located at the MoS_2 edges[8]. Therefore, our materials are more defective on the edges, which is key for the molecular bridging of adjacent flakes and formation of covalently interconnected TMD networks.



Supplementary Fig. 2 | HAADF-STEM investigation. HAADF-STEM images and related histograms of Mo-Mo distance for the **a,** basal plane of LPE-MoS_2, **b,** edge of LPE-MoS_2, **c,** basal plane of MC-MoS_2 and **d,** basal plane of CVD-MoS_2. The histograms show a similar average Mo-Mo distance for the basal plane of all samples, with a significant decrease of ~30 pm for the edge of LPE-MoS_2, pointing to a higher defect density.

3. Morphological and structural investigations

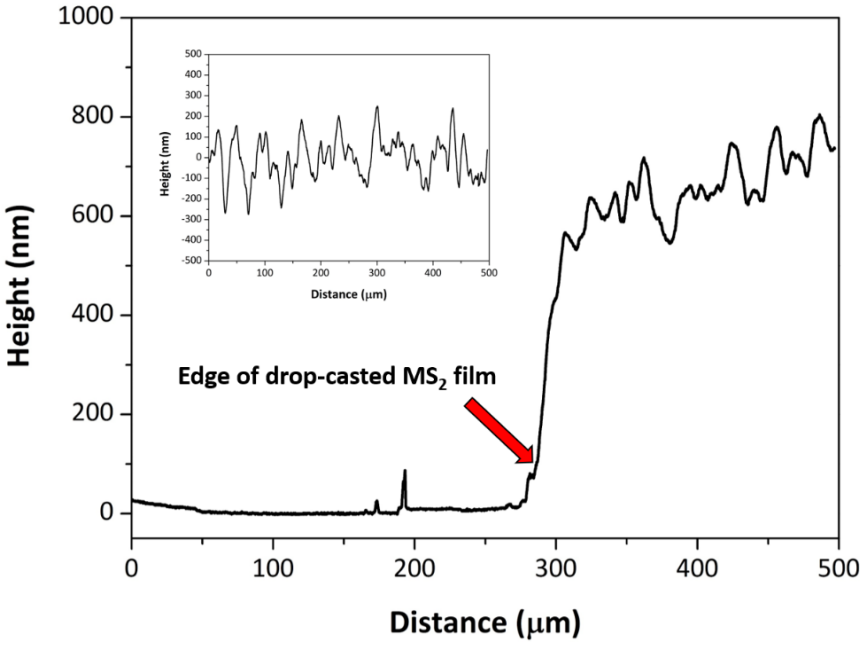
In order to investigate the V_S healing process, we examine and compare the results from AFM and SEM imagining. As shown in Supplementary Fig. 3, no differences are observed between the morphology of MS_2 films and networks (upon BDT treatment). Both exhibit average root-mean-square roughness R_{rms} = 95 ± 10 nm (estimated by AFM mapping over 25 μm^2) and considerable high local disorder. No molecular aggregates or macroscopic post-functionalization effects are observed. The thickness of the drop-cast films is estimated by profilometry, with an average value ~700 ± 100 nm and R_{rms} ~80 ± 20 nm (Supplementary Fig. 4) over a 500 µm sampling distance, in good agreement with AFM data. Also in this case, no remarkable differences are observed before and after BDT treatment.



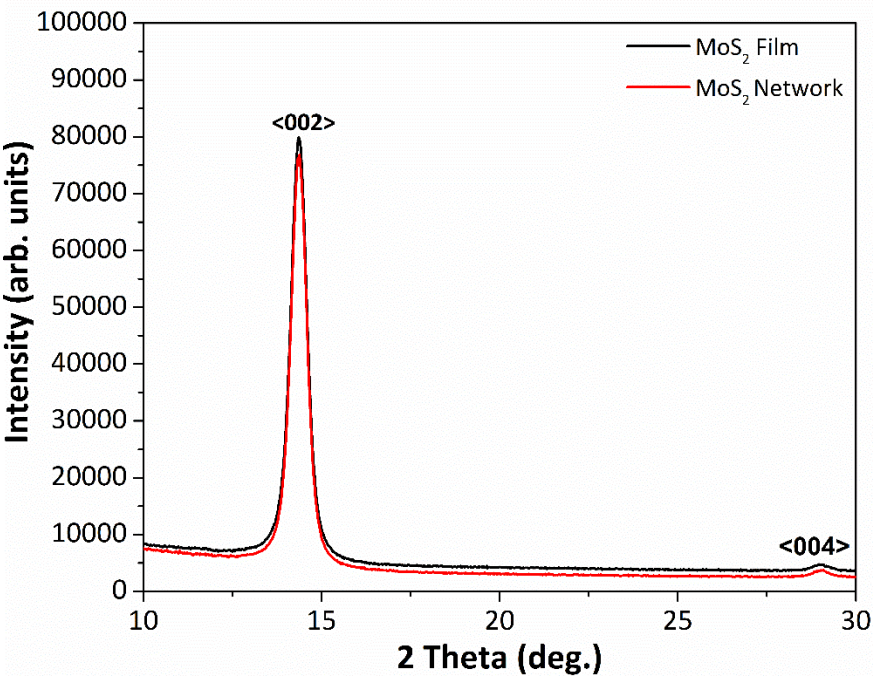
Supplementary Fig. 3 | Surface morphology of MoS_2 films and networks. AFM (top) and SEM (bottom) images for **a**, MoS_2 films and **b**, MoS_2 networks. No significant changes are observed upon BDT functionalization. The SEM images are recorded in-between Au IDEs of pre-patterned SiO_2/Si substrates.

XRD analysis is then used to detect any possible changes due to BDT functionalization. The two diffractograms in Supplementary Fig. 5 display the same characteristic peaks at 14.5° and 29°,

corresponding to the (002) and (004) planes of hexagonal MoS_2, respectively[9]. Therefore, no structural changes are observed upon BDT exposure (*e.g.* intercalation), indicating a preserved crystal structure (Supplementary Fig. 5). We speculate the same rationalizations apply to WS_2 and ReS_2 (XRD data not reported).



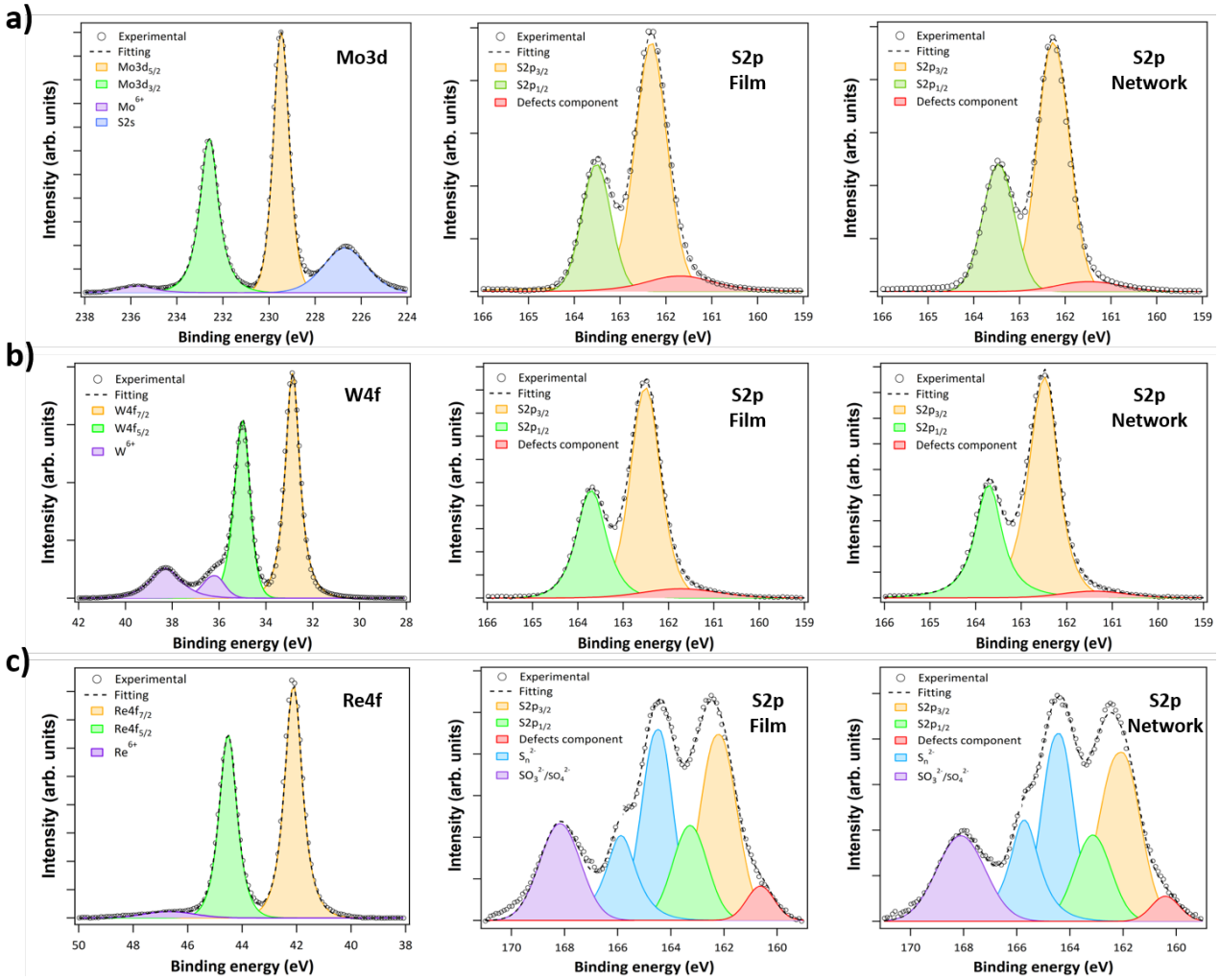
Supplementary Fig. 4 | Thickness and large-scale roughness of MoS_2 films. Profilometer trace of drop-cast MoS_2 film. Inset: Roughness recorded over 500 μm sampling distance.



Supplementary Fig. 5 | XRD analysis of MoS_2 films and networks. Comparison of MoS_2 diffractograms obtained for films (black) and networks (red), displaying the characteristic features.

4. X-ray photoelectron spectroscopy (XPS) analysis

XPS is performed to confirm the V_S healing process, monitoring the evolution of the component (singlet) ascribed to the substoichiometric MS_{2-x} materials (defects component) located ~1 eV lower than the $S2p_{3/2}$ component[10]. Supplementary Fig. 6 shows that the defects component contribution in the S2p spectra diminishes upon BDT exposure and network formation, indicating that the treatment with thiolated molecular systems decreases the defect density in solution-processed MS_2.



Supplementary Fig. 6 | XPS characterization of MS_2 films and networks. a, MoS_2, with Mo3d (left) and S2p regions, the latter for film (middle) and network (right). **b**, WS_2, with W4f (left) and S2p regions, the latter for film (middle) and network (right). **c**, ReS_2, with Re4f (left) and S2p regions, the latter for film (middle) and network (right).

Supplementary Fig. 6 indicates that the defects component (red) decreases after BDT treatment for all MS_2 materials which undergo V_S healing. The ratio of the defects component area (A_{DC}) to the overall S2p region area (A_{S2p}) decreases after BDT exposure. Solution-processed MoS_2 shows the

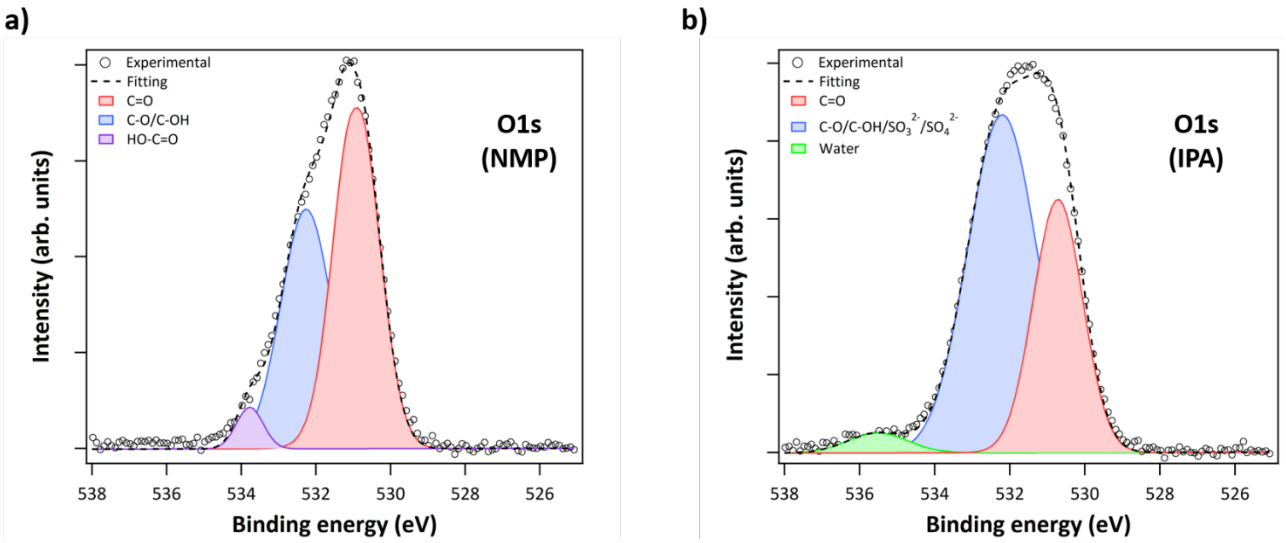
largest variation of A_{DC}/A_{S2p} upon network formation among all MS_2 under analysis (Supplementary Table 2).

TMD	A_{DC}/A_{S2p} Film	A_{DC}/A_{S2p} Network
MoS_2	8.0 ± 0.5 %	5.0 ± 0.5 %
WS_2	6.0 ± 0.5 %	4.0 ± 0.5 %
ReS_2	4.0 ± 0.5 %	3.0 ± 0.5 %

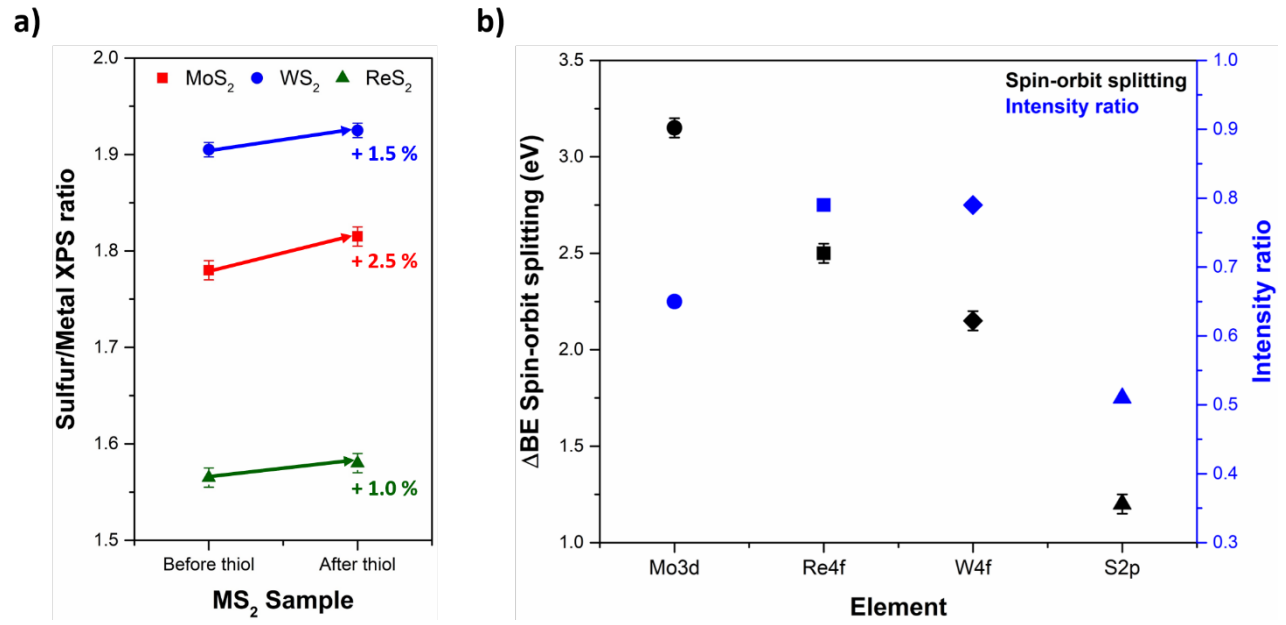
Supplementary Table 2: Defects component weight in high resolution XPS S2p spectra for both films and networks.

We believe that MoS_2 exhibits such a behaviour since it is the material, amongst the three under study, with the best trade-off between high-defectiveness and less oxidized vacancies/lower degree of oxidation, as reported in Supplementary Fig. 6. XPS spectra of WS_2 display two additional components (doublet) at ~36 eV and ~38 eV in the W4f region (besides the $W4f_{7/2}$ and $W4f_{5/2}$ components located at ~33 eV and ~35 eV, respectively), ascribed to W atoms with a 6+ oxidation state[11]. Similar results are observed in the Re4f and S2p regions of the ReS_2 spectra, where many additional intense components are observed and ascribed to oxidized species, such as Re atoms with a 6+ oxidation state, polysulphides (doublet), sulphite and sulphate groups (singlet) coming from the oxidation reactions occurring during the exfoliation procedures[12,13]. ReS_2 is produced by sonicating the starting crystals in IPA, which can promote stronger oxidation reactions than NMP used for MoS_2 and WS_2. Supplementary Fig. 7 compares the O1s XPS regions of MoS_2 and ReS_2, indicating higher amount of oxygen (from half to one order-of-magnitude) in ReS_2 than MoS_2. The O1s region of ReS_2 displays a broader peak, whose components can be fitted according to the oxidation products present in the material upon exfoliation. The C-O components in Supplementary Fig. 7 are assigned to external contaminants, such as solvent traces and adsorbates. MoS_2 has less oxidized V_S than WS_2 and ReS_2, therefore it is more prone to undergo V_S healing reactions, although BDT treatment effects are still evident in all the three materials.

To confirm the effects of thiol functionalization, we survey the evolution of the Sulfur/Metal (S/M) XPS ratio of MS_2 before and after exposure to BDT molecules. Supplementary Fig. 8 shows an increase of S/M upon treatment, supporting the V_S healing mechanism and the decrease of defect density once thiolated molecules are employed.



Supplementary Fig. 7 | XPS O1s region for solution-processed MoS_2 and ReS_2. Solution-processed **a**, MoS_2 and **b**, ReS_2 produced by sonicating the starting bulk material in NMP and IPA, respectively.

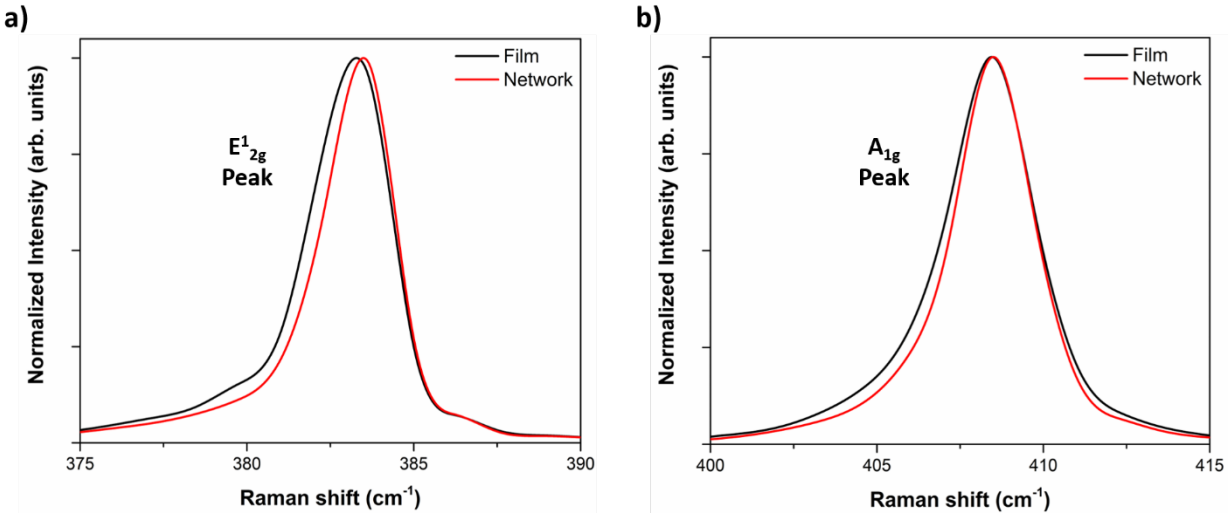


Supplementary Fig. 8 | XPS analysis. a, Sulfur/Metal XPS ratio before and after exposure to BDT molecules for MoS_2, WS_2 and ReS_2. **b**, Summary of the XPS constraints (spin-orbit splitting and intensity ratio) implemented for the fitting of Mo3d, Re4f, W4f and S2p regions, before and after exposure to BDT molecules.

For the sake of clarity, we implement the following constraints in the XPS analysis and fitting procedure using doublets (Supplementary Fig. 8b): i) Mo3d, spin-orbit splitting = 3.15 ± 0.05 eV and intensity ratio = 0.65; ii) Re4f, spin-orbit splitting = 2.50 ± 0.05 eV and intensity ratio = 0.79; iii) W4f, spin-orbit splitting = 2.15 ± 0.05 eV and intensity ratio = 0.79; iv) S2p, spin-orbit splitting = 1.20 ± 0.05 eV and intensity ratio = 0.51.

5. Raman spectroscopy analysis

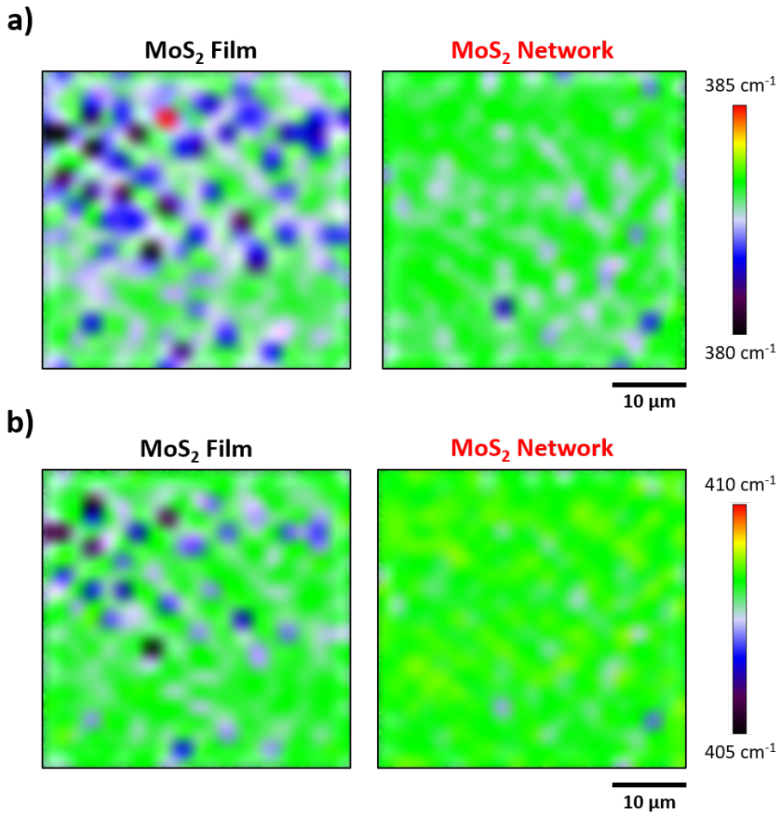
Raman spectroscopy indicates that the Full Width at Half Maximum (FWHM) of E^1_{2g} and A_{1g} peaks for MoS_2 spectra decreases upon thiol exposure (Supplementary Fig. 9). This may be due to the reduction of defect density and, in particular, to the attenuation of defect-activated modes[14].



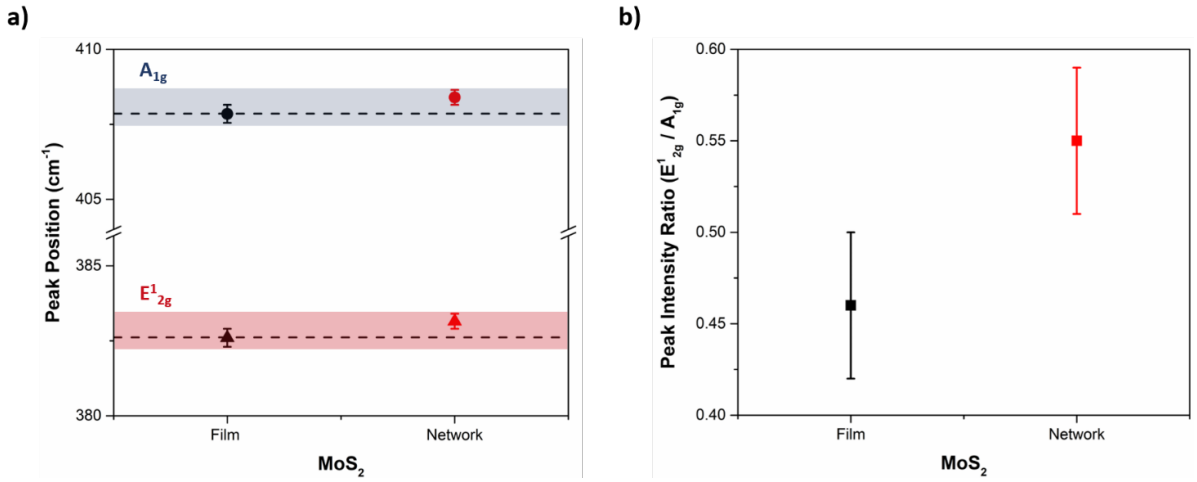
Supplementary Fig. 9 | Raman spectra of MoS_2 films and networks. Comparison between **a**, E^1_{2g} and **b**, A_{1g} peaks for pristine MoS_2 films (black) and networks (red).

We perform a statistical analysis by collecting ~2000 spectra and mapping a total area of ca. 6000 μm^2. Supplementary Fig. 10 shows that, even though both films and networks are continuous, the latter exhibit higher homogeneity. The mapping gives a consistent (~10 %) decrease of FWHM for both E^1_{2g} and A_{1g} peaks upon BDT exposure: E^1_{2g} FWHM decreases from 2.95 ± 0.20 cm^{-1} (films) to 2.50 ± 0.10 cm^{-1} (networks), while A_{1g} FWHM from 3.15 ± 0.15 cm^{-1} (films) to 2.85 ± 0.10 cm^{-1} (networks), as expected when defect density is reduced[14].

We also observe a consistent blue shift of both E^1_{2g} and A_{1g} peaks: from 382.60 ± 0.30 cm^{-1} (films) to 383.20 ± 0.25 cm^{-1} (networks) and from 407.80 ± 0.30 cm^{-1} (films) to 408.40 ± 0.25 cm^{-1} (networks), respectively (Supplementary Fig. 11a). Such small variations are in agreement with the suppression of defects-activated modes and rule out any possible charge transfer phenomena (doping) due to BDT molecules[15]. We then consider the $I(E^1_{2g})/I(A_{1g})$ intensity ratio before and after exposure to thiolated molecules. Supplementary Fig.11b indicates that $I(E^1_{2g})/I(A_{1g})$ increases from 0.46 ± 0.04 (films) to 0.55 ± 0.04 (networks), consistent with previous reports indicating a lower defect density for higher $I(E^1_{2g})/I(A_{1g})$[16].



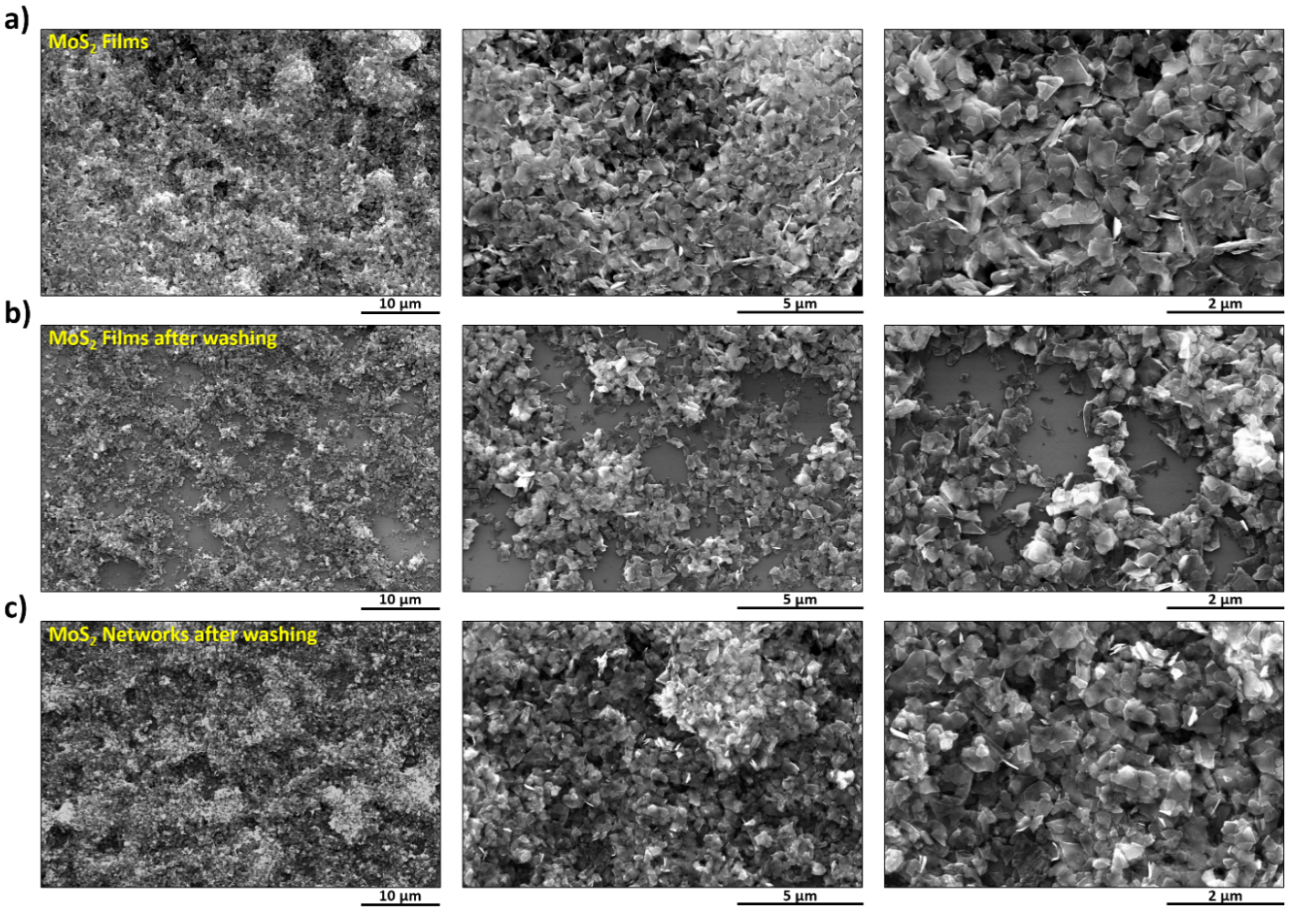
Supplementary Fig. 10 | Raman mapping for MoS_2 films and networks. Raman mapping of **a**, Pos(E^1_{2g}) and **b**, Pos(A_{1g}) for MoS_2 films and networks. Each map contains 441 spectra and covers 1600 µm^2.



Supplementary Fig. 11 | Statistical Raman analysis for MoS_2 films and networks. Fitted **a**, Pos(E^1_{2g}) and Pos(A_{1g}) and **b**, I(E^1_{2g})/I(A_{1g}) for MoS_2 films and networks.

6. Multiscale characterization of functionalized MoS_2 films

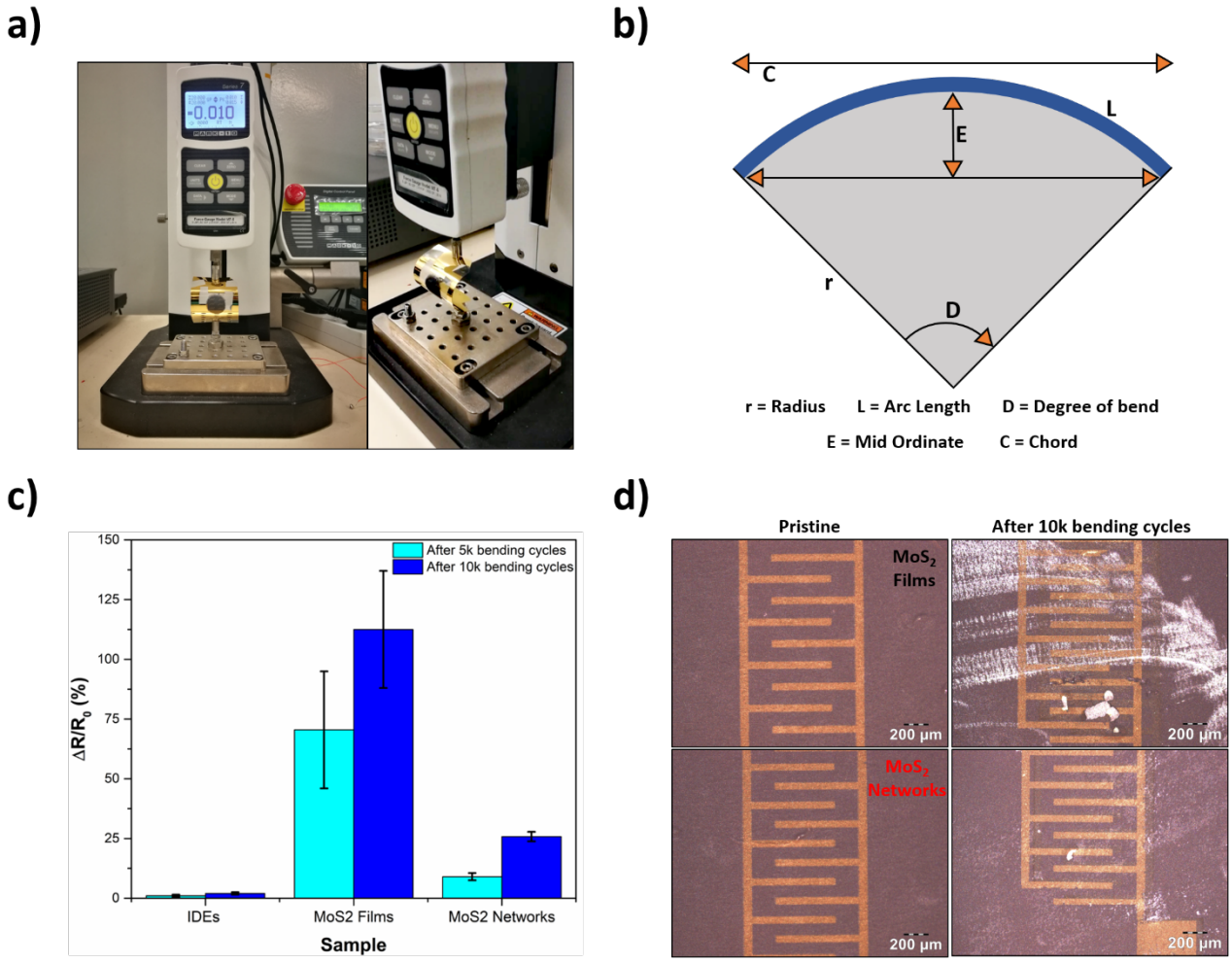
A consequence of the network formation is that MS_2 networks exhibit no significant material detachment upon water exposure (Supplementary Fig. 12), contrary to pristine films, that undergo material loss from the substrate surface. The covalent interconnected system is less soluble and prone to solvation than free single MoS_2 flakes, especially using linkers that present a strong hydrophobic core such as BDT molecules (Supplementary Table 3).



Supplementary Fig. 12 | Water stability. SEM images at different magnifications of **a**, MoS_2 pristine films **b**, MoS_2 pristine films after water exposure and **c**, MoS_2 networks after water exposure.

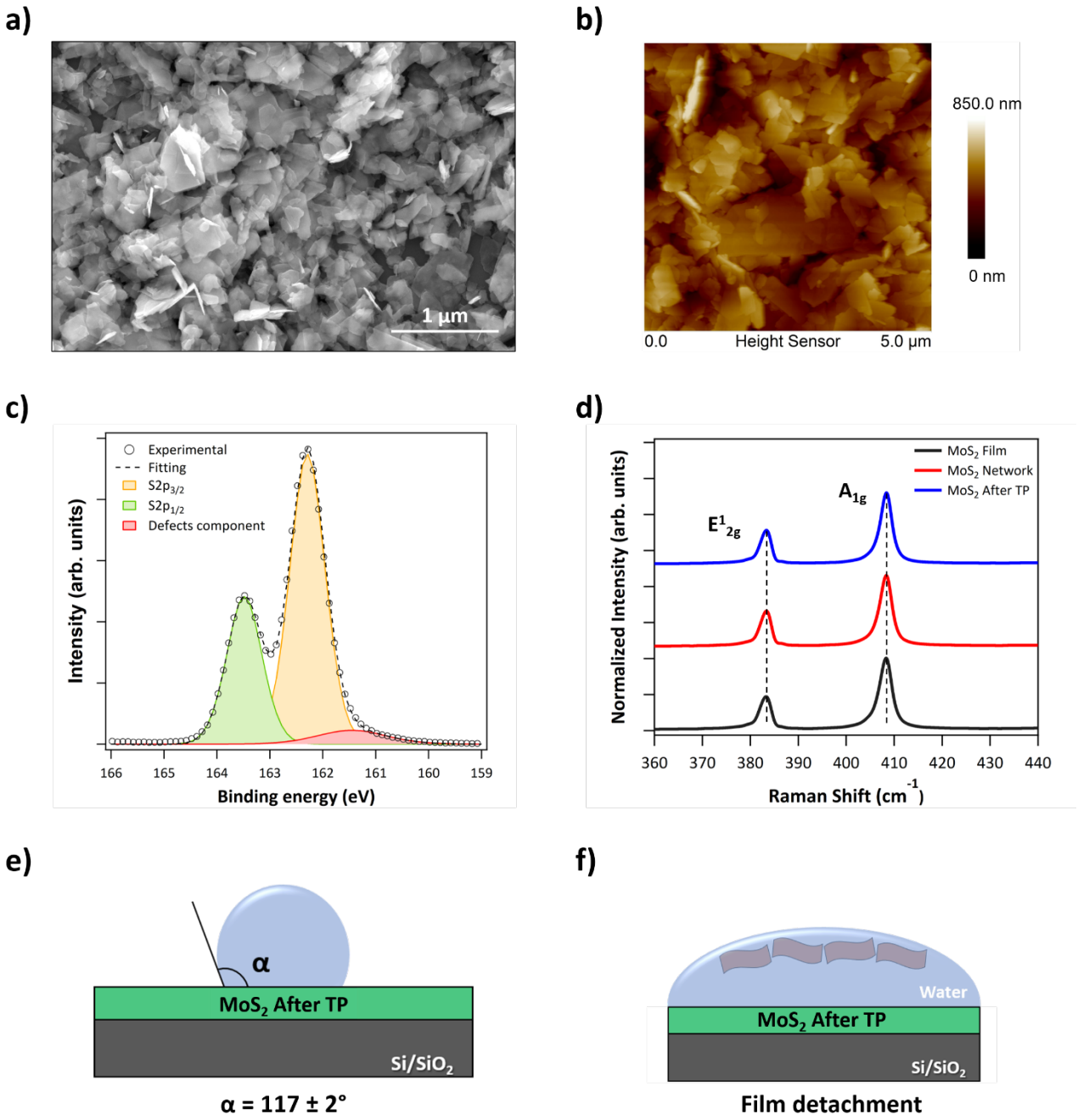
We then investigate the mechanical robustness and consequent electrical stability of MoS_2 films and networks deposited onto flexible polyethylene terephthalate (PET) substrates. We deposit MoS_2 films on PET slides (2 cm x 4 cm) *via* dry-transfer from a polytetrafluoroethylene (PTFE) membrane filter (Φ = 25 mm). After filtering 2 ml of MoS_2 dispersion at 0.6 mg/ml, the filters are pressed against the PET substrates for 1h, with a laboratory manual press. Thus, IDEs are placed onto the film surface by shadow mask evaporation approach, having 5 nm of Cr adhesive layer and 75 nm of Au.

For the production of networks, MoS_2 films are exposed to BDT before the electrode fabrication step. For the mechanical investigation, we set an overall deformation of 2 cm, bending radius (r) = 1 cm and degree of bend (D) = 210°, as illustrated in Supplementary Fig. 13. As shown in Supplementary Fig. 13c, the electrical resistance (R) of the samples increases upon multiple (5k and 10k) bending cycles due to crack formation within both MoS_2 films and networks (Supplementary Fig. 13d). However, MoS_2 networks exhibit superior robustness, characterized by significantly lower variations of relative channel resistance ($\Delta R/R_0$) with respect to pristine films. This supports network formation, whereby a covalent interconnected system possesses superior mechanical robustness, fatigue resistance, and electrical properties.



Supplementary Fig. 13 | Mechanical test. a, Experimental setup. **b**, Sketch of the samples subjected to bending deformation. **c**, Variation of the relative channel resistance $\Delta R/R_0$ of bare IDEs, MoS_2 films, and MoS_2 networks upon 5k and 10k bending cycles, along with related **d**, optical images of MoS_2 films and networks before (left) and after (right) mechanical deformation.

We also perform multiscale characterizations on MoS_2 samples upon exposure to monothiolated molecules, such as TP, with an overall equivalent concentration of functional thiol groups as BDT (Supplementary Fig. 14). An identical *in-situ* approach is used for the functionalization steps (Fig.1a, main text), soaking the samples within a 100 mM solution of TP in anhydrous hexane under N_2-controlled atmosphere.



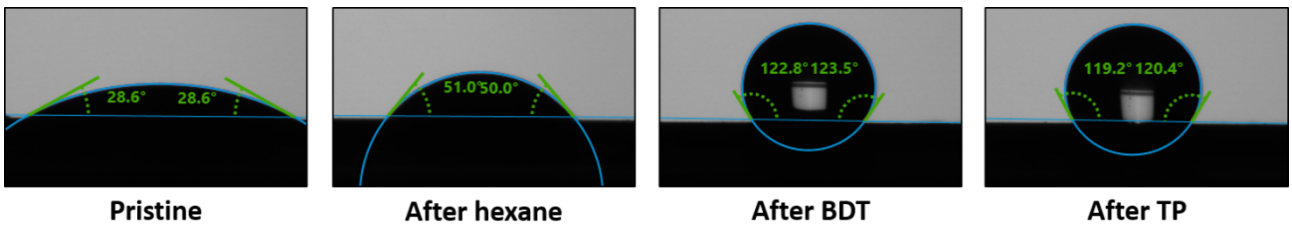
Supplementary Fig. 14 | Multiscale characterization of MoS_2 films exposed to TP molecules. a, SEM and **b**, AFM images upon TP exposure. **c**, HR-XPS S2p spectrum. **d**, Raman spectra of MoS_2 films, networks and TP-functionalized films. **e**, Schematic illustration of the static water contact angle results and **f**, water stability test.

Morphological and structural characterizations, based on AFM and SEM imaging, indicate no significant differences between pristine films, networks and TP-functionalized films, as expected for a molecular-level chemical functionalization.

XPS confirms the V_S healing process, since the defects component deconvoluted from the S2p high-resolution spectra decreases upon TP exposure. The ratio of the defects component area to the overall S2p region diminishes after functionalization, from 8.0 % to 5.0 % analogously to the BDT case (see Section 4). This confirms the decrease of defect density when thiolated molecules are employed to heal V_S in solution-processed MS_2.

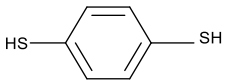
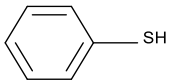
A further evidence of V_S healing comes from the Raman analysis. FWHM (E^1_{2g}) and FWHM (A_{1g}) decreases upon thiol exposure, both for MoS_2 networks and TP-functionalized films (see Section 5). Ultimately, the treatment with thiolated molecules promotes the healing of V_S, thereby attenuating the defect-activated modes[14].

Static water contact angle measurements show a shift of the average contact angle upon thiol exposure, both BDT and TP (Supplementary Fig. 15). Due to the similar molecular structure of the two functionalizing agents — they differ just for one thiol group — a similar hydrophobic behaviour is expected for BDT-linked networks and TP-functionalized films. The results are summarized in Supplementary Table 3 and support network formation and the consequent increased connectivity due to the bridging of adjacent flakes (after BDT), since the presence of free thiol groups would have shifted the samples towards a more hydrophilic character[17].



Supplementary Fig. 15 | Static water contact angle. Optical images with contact angle analysis of pristine MoS_2 films and upon thiol exposure, both BDT and TP. An additional test is performed to rule out effects due to the solvent used during functionalization reaction (hexane).

MoS_2 films are not stable in water and detachment is observed. Thus, contact angle measurements are performed recording the values during the initial stage of the wetting procedure (< 30 s) on fresh samples to ensure repeatability and reproducibility.

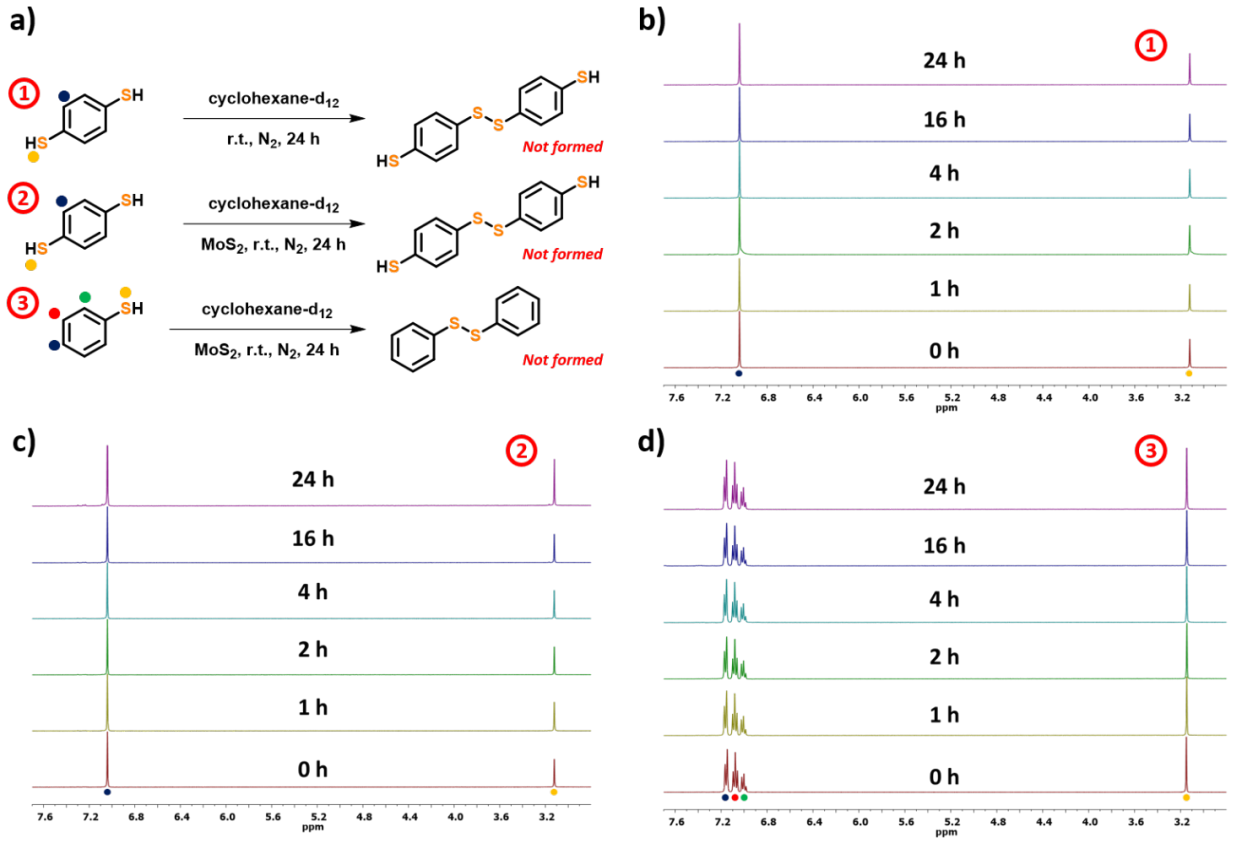
MoS_2 (Drop-cast)	Average Static Contact Angle (°)
Pristine (Film)	30 ± 3
After hexane	53 ± 2
After BDT (Network) 	121 ± 2
After TP 	117 ± 2

Supplementary Table 3: Static water contact angle for MoS_2 films upon different treatments. The standard deviation values, for each sample, are estimated from 10 independent measurements.

Similarly to the pristine systems, TP-functionalized MoS_2 films display poor water stability and film detachment is observed. Therefore, dithiolated molecules, such as BDT, are needed for network formation and production of water-stable materials. Once the MoS_2 flakes are linked, they behave as interconnected network, less soluble and able to withstand solvation processes promoted by the aqueous environment.

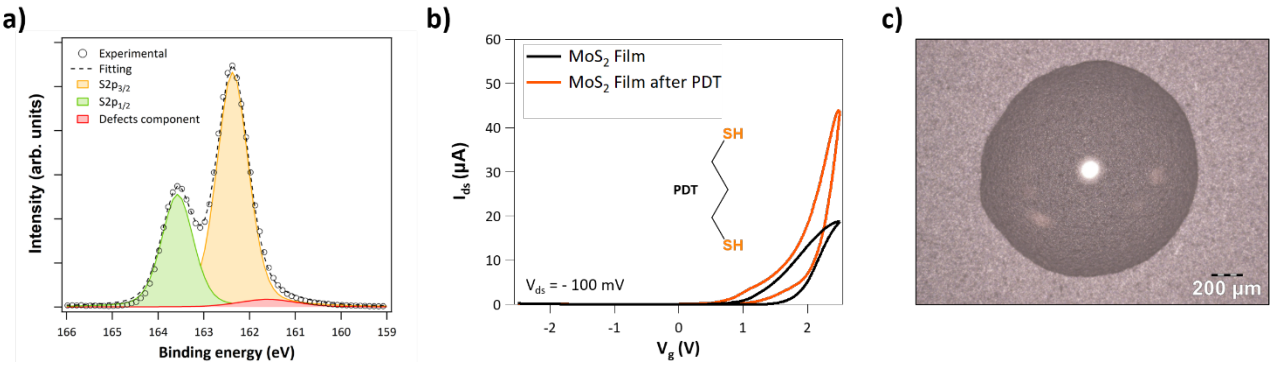
We believe that the same observations arising from the results of TP-functionalized MoS_2 samples can be extended to WS_2 and ReS_2, due to the similar reactivity and physicochemical properties of these systems[18,19].

To further investigate the reaction between MoS_2 and thiols (BDT and TP), we perform Nuclear magnetic resonance (NMR) mimicking the same operating conditions employed for network formation. Hence, we carry out the reaction under N_2-controlled atmosphere, at room temperature and using a non-polar solvent. MoS_2 (3 mg, 0.02 mmol) is sonicated in cyclohexane-d_{12} (2ml) for 10 mins prior to adding BDT (15 mg, 0.10 mmol) and stirring the solution for 24h. At the same time, a control experiment in absence of MoS_2 is performed. Supplementary Fig. 16 shows the NMR spectra related to the reaction between MoS_2 and BDT acquired 1, 2, 4, 16, 24h after the addition of thiolated molecules. No disulfide species are formed under any circumstances[20], ruling out dimerization, and supporting the functionalization reaction as pathway governing the V_S healing[21,22]. Analogous results are obtained for TP.



Supplementary Fig. 16 | NMR investigation. a, Tested reactions between MoS_2 and thiolated molecules under exam (TP and BDT). Related NMR spectra at different time intervals for **b**, control experiment (BDT without MoS_2), **c**, MoS_2 + BDT and **d**, MoS_2 + TP.

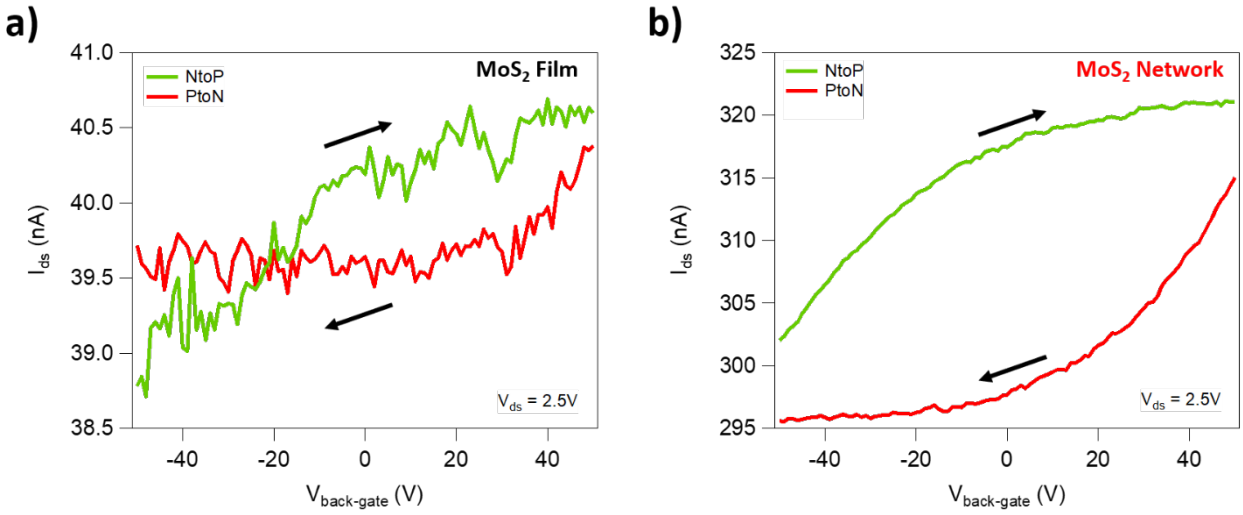
We then test the effects of the linker structure on the properties of MoS_2 networks. For this purpose, we use a dithiolated molecular system with an aliphatic chain: propane-1,3-dithiol (PDT). As for Supplementary Fig. 17, PDT functionalization leads to network formation, where the final material exhibits lower defect density, improved electrical performance and water stability (further details about the electrical characteristics are in Section 7).



Supplementary Fig. 17 | Multiscale characterization of MoS_2 networks obtained *via* PDT linkers. a, HR-XPS of the S2 region for MoS_2-PDT networks. **b**, LG-TFT characteristics for MoS_2 pristine films and MoS_2-PDT networks. **c**, Optical image showing the inherent water stability of MoS_2-PDT networks.

7. Electrical properties of thin-film transistors

In order to prove an extensive penetration of functionalizing molecules through the whole film, we evaluate the electrical properties of MS_2 films exposed to BDT by measuring back-gated TFTs, probing the charge carrier transport at the device SiO_2 bottom interface. As shown in Supplementary Fig. 18, the exposure to dithiolated molecules promotes an enhancement of electrical performance comparable to that reported in Fig. 3 of the main text. Field-effect mobility (μ_{FE}) increases by one order-of-magnitude with respect to pristine films. This is consistent with V_S passivation and interflake bridging by BDT molecules *via* diffusion throughout the whole film. Supplementary Fig. 18 also shows the typical limitations of TMD back-gated TFTs (*e.g.*, low current ratios, scant absolute μ_{FE}, large hysteresis), thereby supporting our choice to focus on LG-TFT to assess the network formation.



Supplementary Fig. 18 | Electrical characterization of back-gated TFTs. Transfer curves for MoS_2 TFTs based on **a**, films and **b**, networks in back-gate configuration. All curves are recorded at V_{ds} = 2.5 V and sweeping $V_{back\text{-}gate}$ from -50 to + 50 V.

In order to probe the excess of thiolated molecules during the functionalization steps, we measure the TFT characteristics of MoS_2 samples exposed to two rounds of BDT. No significant changes in μ_{FE} are observed upon a second exposure to BDT (Supplementary Table 4), confirming that one functionalization step, for our experimental conditions, is sufficient to saturate and heal V_S, maximizing the number of molecules used to bridge adjacent flakes.

Sample	μ_{FE} / $\mu_{FE, Film}$
MS_2 Film	1
After BDT (1st functionalization)	10 ± 1
After BDT (2nd functionalization)	10 ± 1

Supplementary Table 4: Variations of μ_{FE} for MoS_2-based TFTs before and after single and double exposure to BDT.

As reported in the main text, network formation results in an enhancement of the electrical properties of MoS_2 LG-TFTs. Such an improvement is reproducible in WS_2 and ReS_2-based devices, proving that V_S healing leads to similar results within TMD interconnected systems (Supplementary Table 5).

TMD	Polarity	μ_{FE} ($cm^2 V^{-1} s^{-1}$)		I_{ON} / I_{OFF}		V_{th} (V)	
		Film	Network	Film	Network	Film	Network
MoS_2	n-type	10^{-3}	10^{-2}	10^3	10^4	1.9 ± 0.1	1.8 ± 0.1
WS_2	n-type	10^{-3}	10^{-2}	10^3	10^4	2.0 ± 0.1	1.9 ± 0.1
ReS_2	n-type	10^{-4}	10^{-3}	10^3	10^4	1.8 ± 0.1	1.8 ± 0.1

Supplementary Table 5: Electrical properties of MS_2-based LG-TFTs. Measurements are performed in a glovebox (N_2-controlled atmosphere), recording I_{ds} while sweeping V_g between - 2.5 and + 2.5 V, with V_{ds} = 100 mV.

Supplementary Table 5 shows minimal variations of V_{th} upon BDT exposure. Our functionalization approach is applied on drop-cast TMD thin films with high defect density, complexity, and disordered nature, whereby grain boundaries and edges dominate the overall charge carrier transport. Therefore, despite our functionalization strategy boosts the overall electrical performance of MS_2 networks by bridging adjacent flakes thanks to dithiolated linkers, V_S has a limited share of the overall

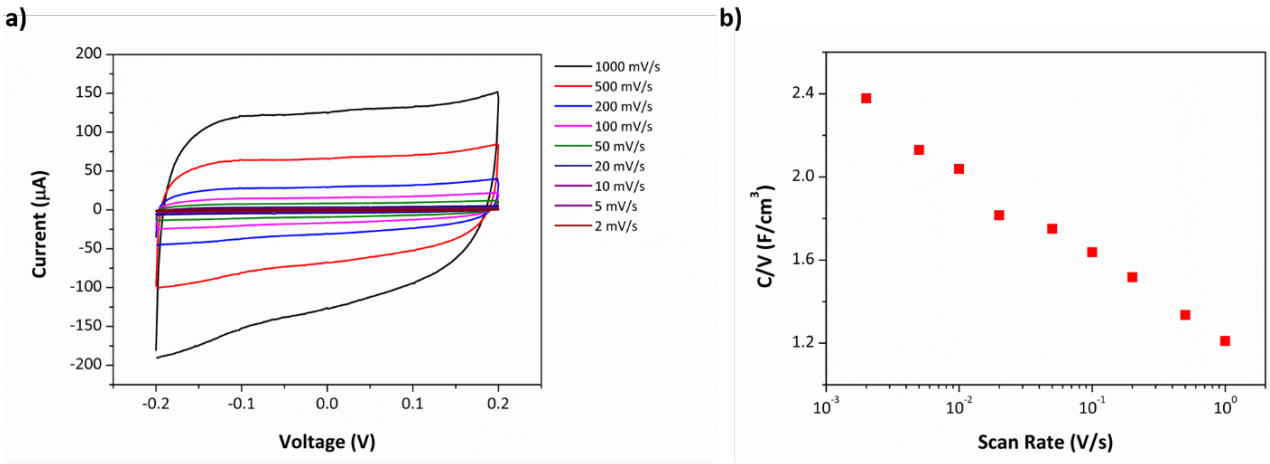
defectiveness of the samples, and it is just one of many factors responsible for the hysteretic behaviour of our devices.

The overall electrical performances are assessed by the figures of merit (FOM) in Supplementary Table 5. μ_{FE} is calculated from the transfer curves (I_{ds} *vs.* V_g) as[23]:

$$\mu_{FE} = \frac{g_m L}{C_v V_{ds} W t} \quad (S1)$$

where g_m is $(\partial I_{ds}/\partial V_g)_{MAX}$, L is the channel length (2.5 μm), C_v is the volumetric capacitance, V_{ds} is the source-drain voltage, W is the channel width (10^4 μm), and t is the film/network thickness.

To estimate C_v, we perform cyclic voltammetry (CV) in a three-electrode cell set-up with a Ag/AgCl reference electrode and a Pt counter electrode. The electrochemical measurements for MoS_2 and WS_2 are in ref. 13. The ReS_2 measurements are done with the same procedure. ReS_2 is spray-coated onto ITO-coated glass to form the working electrode (A ~ 2.3 cm^2, t ~ 400 nm). Each electrode is then submerged in the ionic liquid (EMI-TFSI) (degassed for 12h in a vacuum oven at 70°C). CV is performed in a small (-0.2 V to +0.2 V) voltage window in ambient conditions at different scan rates, Supplementary Fig. 19a.



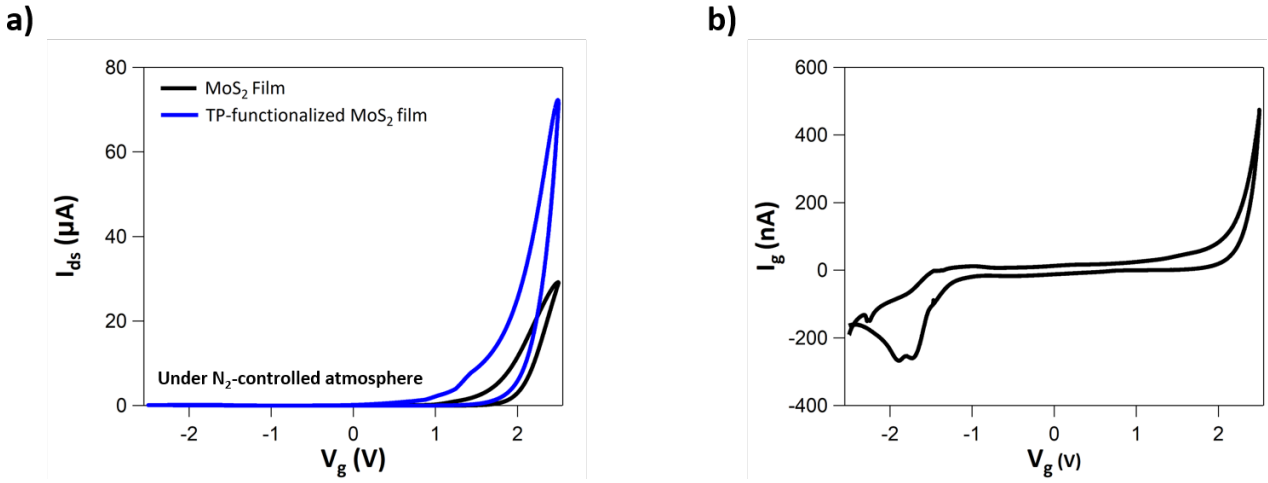
Supplementary Fig. 19 | Electrochemical characterization of ReS_2 films. a, Cyclic voltammograms for ReS_2 films at different scan rates. **b**, Scan rate dependence on sample capacitance.

C_v is calculated as:

$$\frac{C}{V} = \frac{1}{A\, t\, \Delta V\, (\frac{dV}{dt})} \int_{-0.2}^{0.2} I\, dV \quad (S2)$$

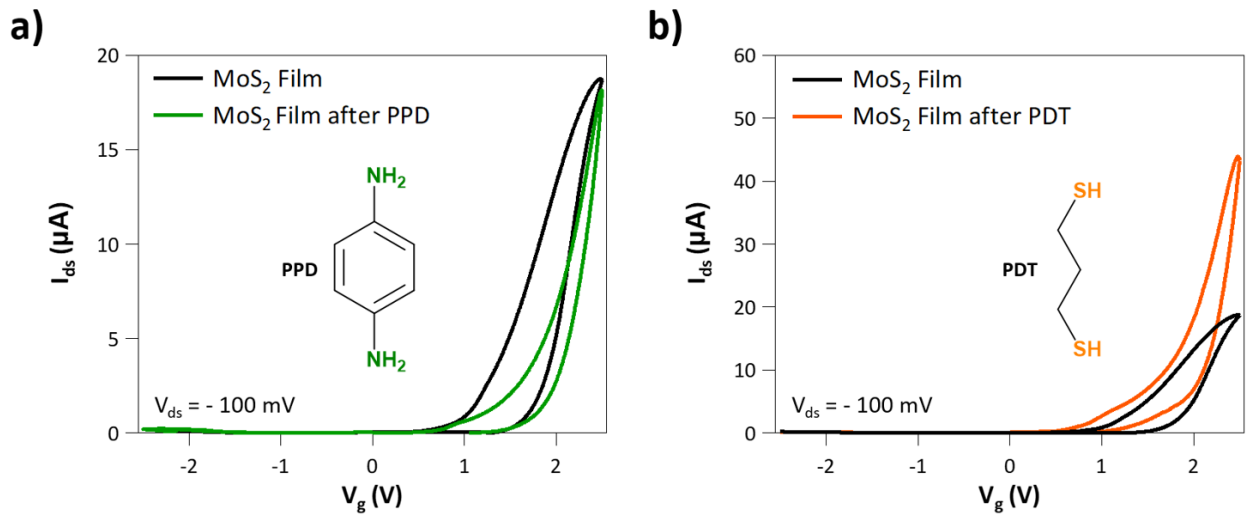
where ΔV is the voltage window and dV/dt is the scan rate in Supplementary Fig. 19b. We get C_v ~2.1 F/cm^3 (at 5 mV/s), similar to the 1.9 and 1.2 F/cm^3 previously measured for MoS_2 and WS_2[23].

We then test the electrical properties of TP-functionalized MoS_2 films. These show a slight increase of performances upon thiol exposure, due to V_S healing (Supplementary Fig. 20). Such a variation is not comparable with the enhancement upon network formation. Networks have μ_{FE} one order-of-magnitude higher than films, whereas TP-functionalized films show higher μ_{FE} by only a factor 2-3.



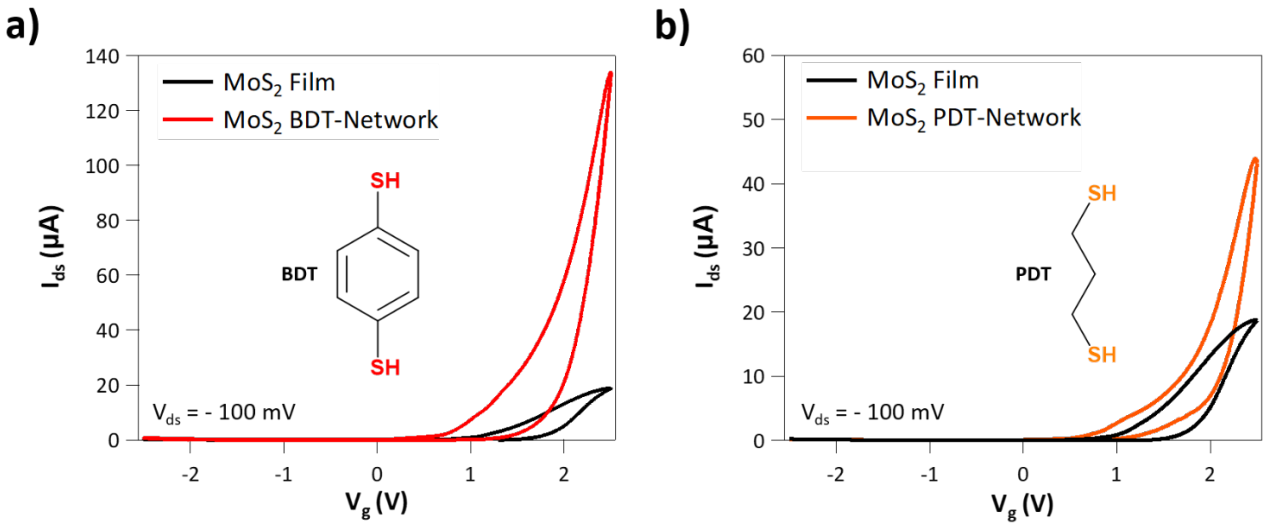
Supplementary Fig. 20 | Electrical characterization. a, Comparison between two typical transfer curves for pristine MoS_2 (black) and TP-functionalized MoS_2 (blue) films. **b**, Typical leakage curve for MoS_2 LG-TFTs. All curves are recorded for V_{ds} = -100 mV and sweeping V_g from -2.5 to +2.5 V.

In order to investigate the effects of the linker structure on the electrical performance of LG-TFTs, we explore the functionalization of MoS_2 films with benzene-1,4-diamine (PPD) and propane-1,3-dithiol (PDT). As for Supplementary Fig. 21a, MoS_2 films exposed to PPD (*i.e.* conjugated core, but no thiol groups) exhibit no improvement of current compared to pristine samples, with only a mild decrease of hysteresis, likely due to the electrostatic screening of charge traps by free PPD trapped molecules within the film[24]. This confirms the need of thiol functional groups to form networks in defective solution-processed MS_2.



Supplementary Fig. 21 | Electrical characterization of MoS_2 films treated with PPD and PDT. Transfer curves for MoS_2 LG-TFTs **a**, before and after treatment with PPD and **b**, before and after treatment with PDT. All curves are recorded at V_{ds} = -100 mV, using EMI-TFSI as electrolyte and a Pt wire as gate electrode. The molecular structures of PPD and PDT are indicated.

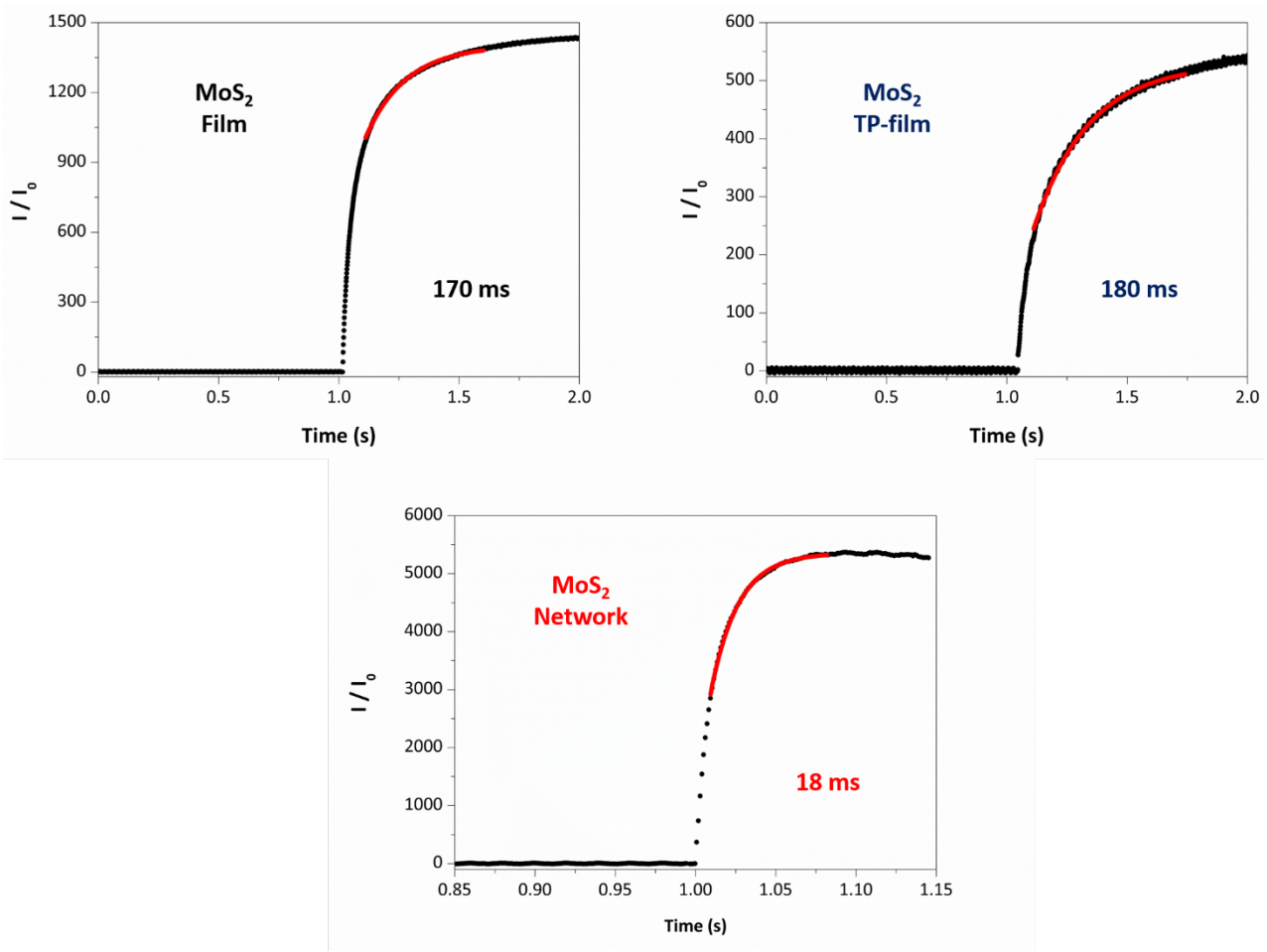
LG-TFTs based on MoS_2 networks functionalized with PDT exhibit current and μ_{FE} 2 to 3-times higher than pristine films (Supplementary Fig. 21b). Nevertheless, the lack of a delocalized electron system in PDT molecules makes such a linker no rival for BDT, with one order-of-magnitude increase in the main figures of merit (Supplementary Fig. 22). This highlights the importance of interflake transport on the ultimate device performance.



Supplementary Fig. 22 | Influence of the linker structure on electrical performance of MoS_2 networks. Transfer curves for MoS_2 LG-TFTs **a**, before and after treatment with BDT linkers and **b**, before and after treatment with PDT linkers. All curves are recorded at V_{ds} = -100 mV, using EMI-TFSI as electrolyte and a Pt wire as gate electrode. The molecular structures of BDT and PDT are also indicated.

We then estimate the switching time (τ_S) for MoS_2-based LG-TFTs upon TP exposure and network formation. TP-functionalized films have τ_S comparable to pristine films, further highlighting the requirement of forming a covalently interconnected system to achieve high electrical performance. τ_S is calculated by fitting (Supplementary Fig. 23) the device transient current, before achieving a steady-state response in the resulting I/I_0 *vs.* time curves, with the non-linear growth equation:

$$I = I_0 + A * e^{-\frac{(t-t_0)}{\tau_S}} \qquad (S3)$$



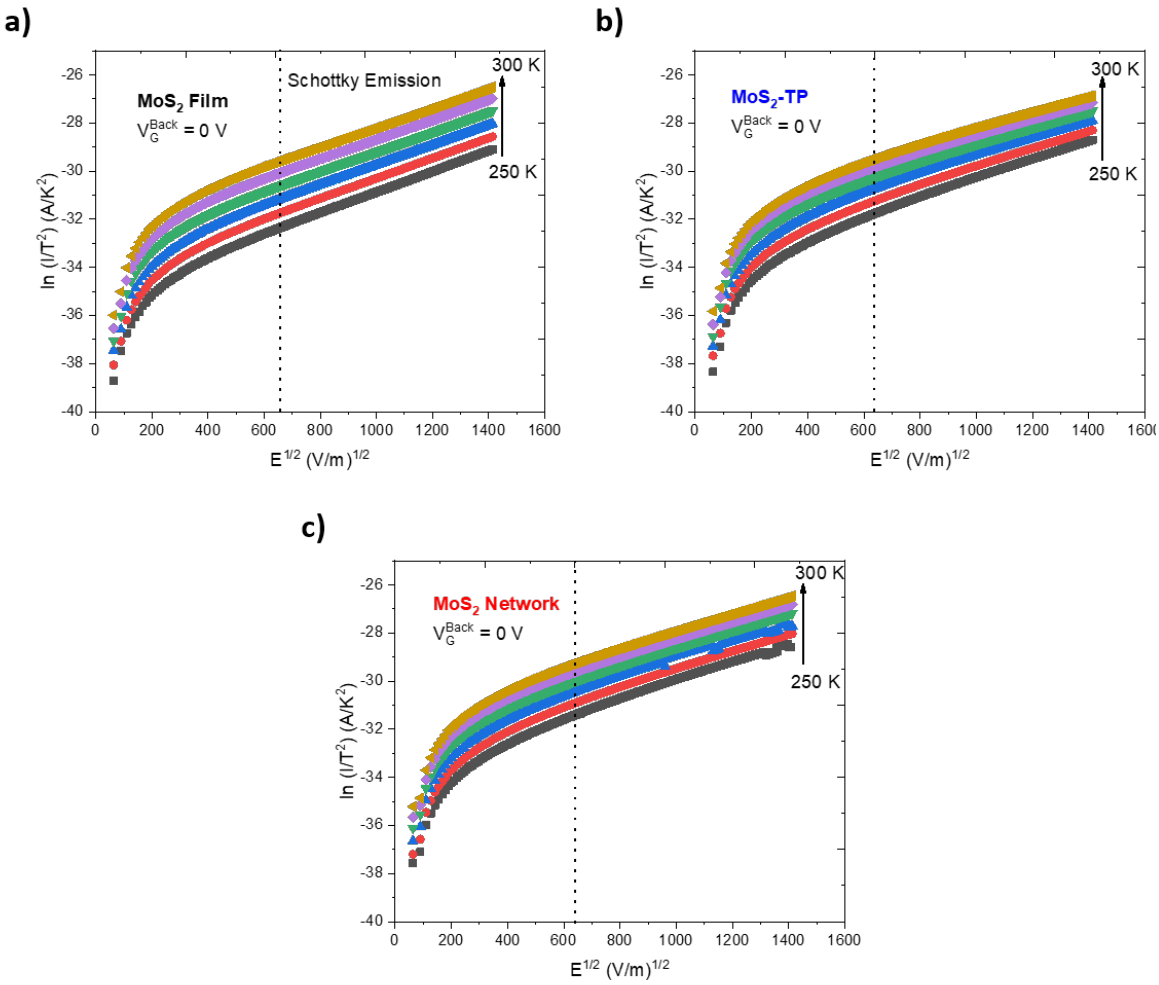
Supplementary Fig. 23 | Switching time measurements. Current *vs.* time curves (normalized to starting current I_0) for MoS_2 films (black), TP-functionalized films (blue) and networks (red) with related τ_S. The red line delimits the range in which a non-linear growth equation can be used to extrapolate τ_S.

8. Temperature-dependent electrical characteristics

To investigate the charge transport mechanisms responsible for the enhancement of electrical properties in MoS_2 networks, we evaluate the electrical characteristics (I-E) before and after thiol functionalization, as a function of temperature (T). Above intermediate E (> 4 x 10^5 V/m), to avoid contact issues related to low fields, and within the T range 250-300 K, MoS_2 pristine films, MoS_2 networks and MoS_2 TP-functionalized samples exhibit I-E characteristics in agreement with Schottky emission[25] (Supplementary Fig. 24), where $\ln(I/T^2)$ is linear with $E^{1/2}$, as for:

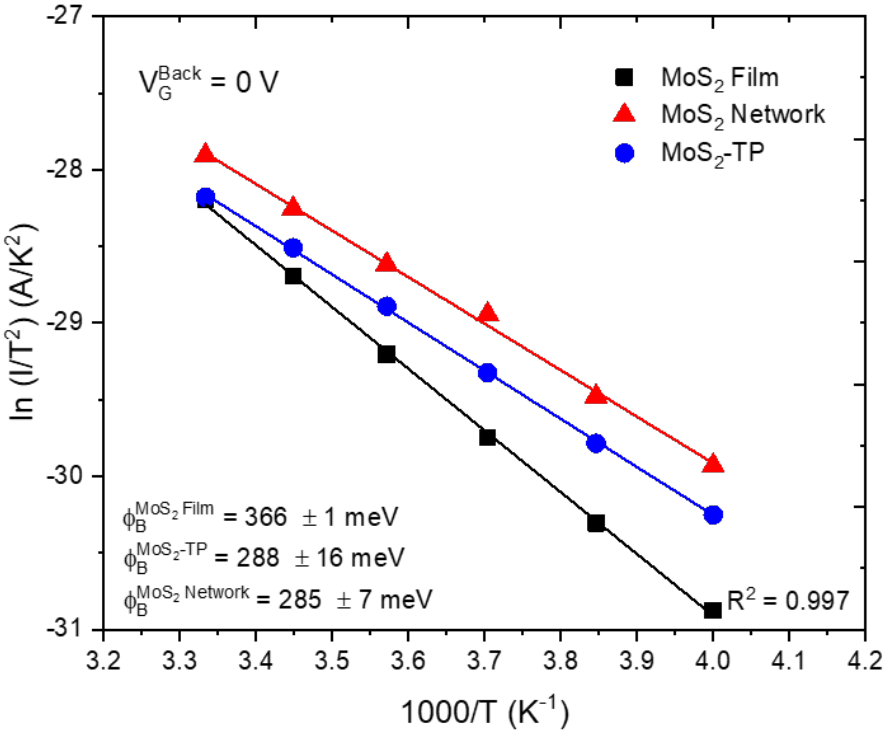
$$I = A A^* T^2 exp\left(\frac{-q\,(\emptyset_B - \sqrt{qE\,/\,4\pi\varepsilon_r\varepsilon_0})}{k_B T}\right) \quad (S4)$$

where A is the charge injection area, A^* is the effective Richardson constant, T is the absolute temperature, k_B is the Boltzmann constant, Φ_B is the Schottky barrier height, ε_r is the MoS_2 dielectric constant (ε_r ~4.8 for multilayer MoS_2 from ref. 26) and ε_0 the free-space permittivity.



Supplementary Fig. 24 | Schottky plots. Ln $I(/T^2)$ *vs.* $E^{1/2}$ for **a**, MoS_2 pristine films **b**, TP-functionalized samples and **c**, MoS_2 networks in a T range 250-300 K without an external gate bias on the back electrode of Si/SiO_2/IDE test patterns.

Considering the slope of ln (I/T^2) *vs.* $E^{1/2}$, we get Φ_B from the Arrhenius plot as in Supplementary Fig. 25.

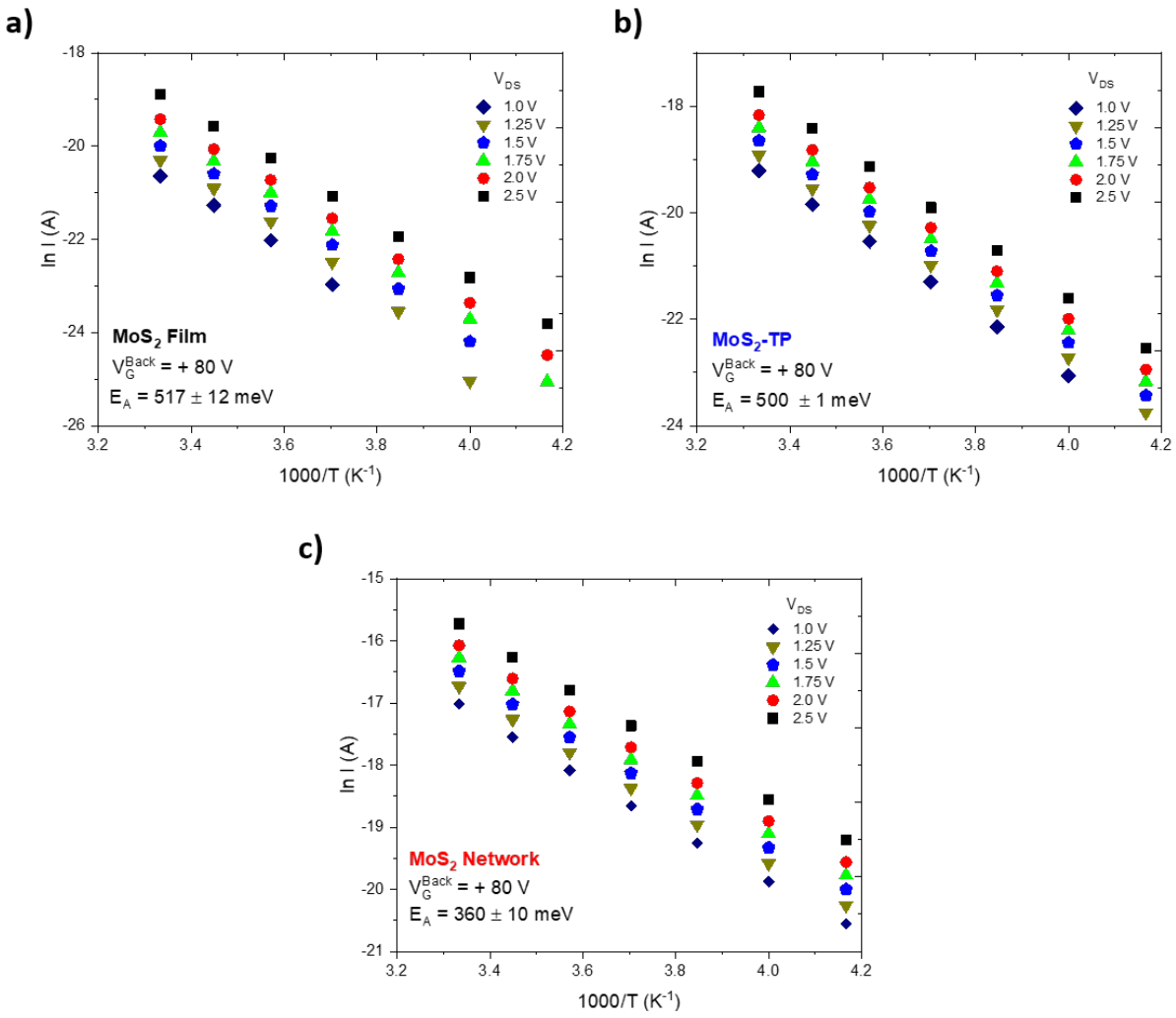


Supplementary Fig. 25 | Arrhenius plot for Schottky emission currents at V_G^{Back} = 0 V. Φ_B calculated from the Schottky formalism for MoS_2 pristine films, TP-functionalized samples and MoS_2 networks. The errors in Φ_B correspond to the standard deviation of values calculated at different E.

We obtain Φ_B = 366 ± 1 meV for MoS_2 films, Φ_B = 285 ± 7 meV for MoS_2 networks, and Φ_B = 288 ± 16 meV for samples treated with monothiolated (TP) molecules. The lower and similar Φ_B for TP- and BDT-functionalized samples, when compared to pristine MoS_2 films, suggest a modification of the Au/MoS_2 interface. Measurements of Au work function (Φ_{WF}) by Photo-Electron Spectroscopy in Air (PESA), before and after thiol treatment, reveal minor changes of the surface characteristics of the electrode (Supplementary Table 6). V_G^{Back} reduces the Au/MoS_2 Schottky barrier, allowing one to probe the bulk electrical properties of the investigated samples[27]. For V_G^{Back} = +80 V, differences in the I-E characteristics of MoS_2 films and networks become noticeable, as discussed in the main text. Within the T range 250-300K and E = 1 MV/m, the samples show a thermally-activated current response with different activation energies (E_A), as illustrated in Supplementary Fig. 26.

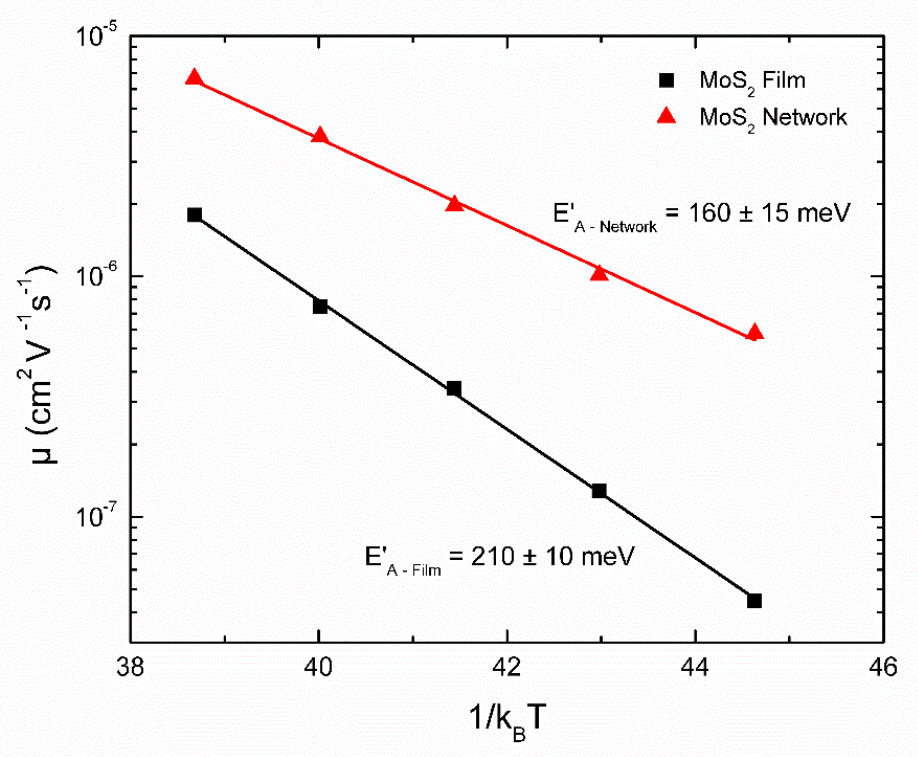
Au Electrodes	Work function (eV)
Bare	5.11 ± 0.02
After Hexane	4.90 ± 0.05
After BDT solution	4.97 ± 0.10
After TP solution	4.93 ± 0.07

Supplementary Table 6: Work function from PESA for Au electrodes in pristine case, after solvent (hexane) exposure and after thiol treatment with BDT and TP molecules. The mean value and standard deviation are estimated from 10 measurements for each sample.



Supplementary Fig. 26 | Thermally-activated current response. Ln I *vs.* 1000/T for V_G^{back} = + 80 V in **a**, MoS_2 films **b**, TP-functionalized samples and **c**, MoS_2 networks. E_A is calculated from the curve slope with errors associated to different applied bias on the IDEs (from 1-2.5 V, i.e., E = 4 x 10^5 – 1 x 10^6 V/m).

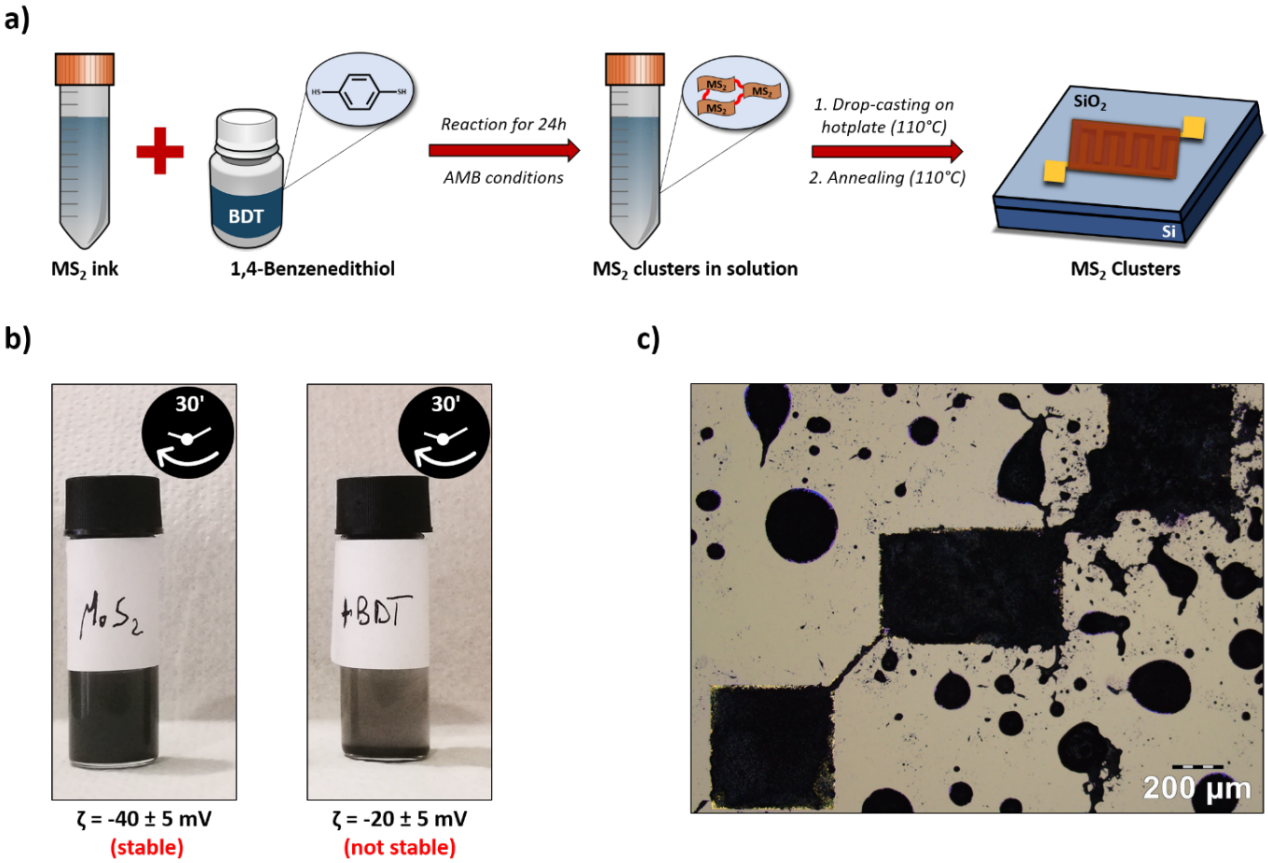
E_A is calculated at different intermediate bias using an Arrhenius relation $I \sim I_0 exp\left(-\frac{E_A}{k_B T}\right)$, where I_0 is an arbitrary initial current. The values for MoS_2 networks (E_A = 360 ± 10 meV) are significantly smaller than for samples where no networks are formed (MoS_2 pristine and TP-functionalized films), corroborating the effect of a covalent link amongst individual MoS_2 flakes. A similar trend is observed by sweeping V_G^{Back}, where the temperature-dependent mobility, μ(T), follows an Arrhenius relation $\mu \sim \mu_0 exp\left(-\frac{E_A}{k_B T}\right)$, with lower E_A for networks than pristine MoS_2 films (Supplementary Fig. 27).



Supplementary Fig. 27 | Mobility Arrhenius plot for MoS_2 films and networks devices in back-gated configuration. The mobility is extracted from the transfer curves for V_{ds} = 5 V and sweeping V_G^{back} from – 60 to + 60 V.

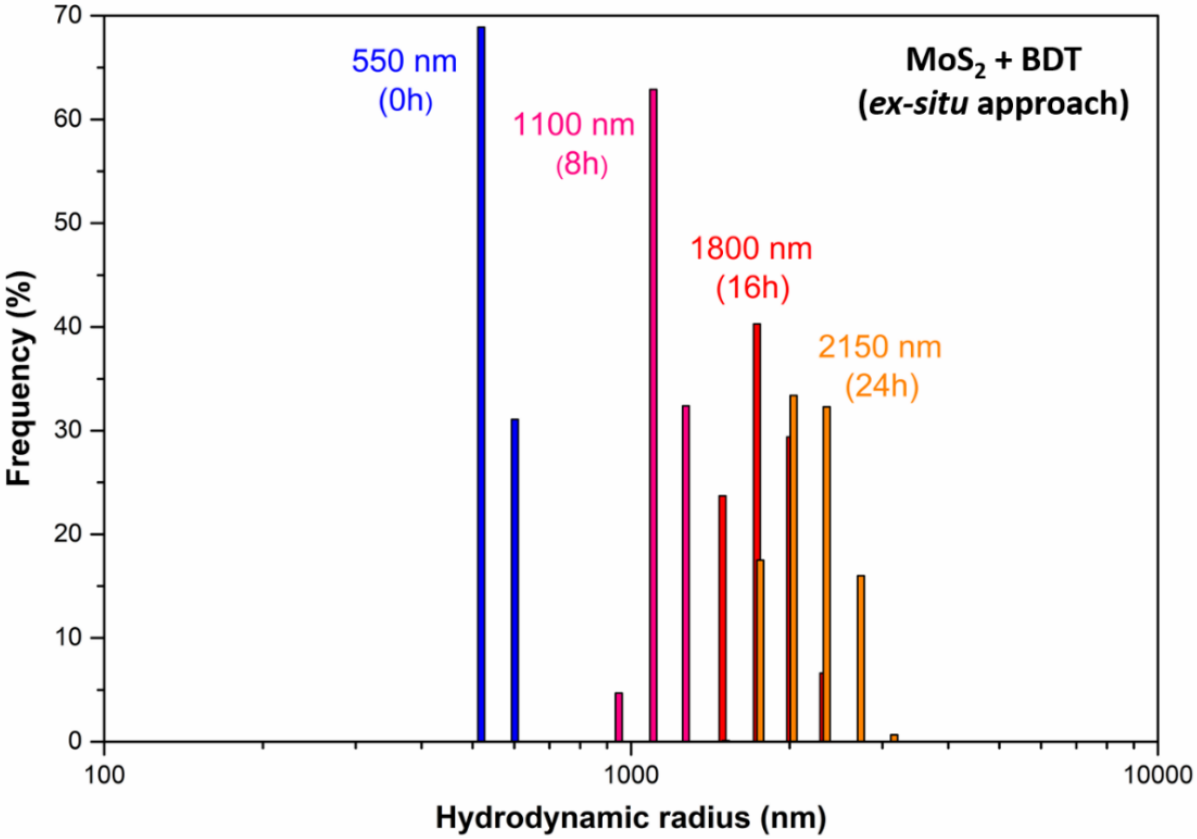
9. Ex-situ functionalization

As counter proof, we perform MoS_2 *ex-situ* functionalization (Supplementary Fig. 28a) by adding BDT molecules directly to the dispersion prior to film casting. The results confirm the need of the *in-situ* approach to produce long-range covalently interconnected TMD networks. The functional *ex-situ* inks have poor stability and start to aggregate within 30-45 mins (Supplementary Fig. 28b) after mixing/sonication. Nevertheless, these inks present excellent patternability for IDEs, promoting an accurate deposition of the material in the contact area (Supplementary Fig. 28c).



Supplementary Fig. 28 | Ex-situ functionalization with BDT. a, Schematic illustration for the *ex-situ* functionalization of MS_2 inks with BDT. **b**, Outcome of stability test for pristine and BDT-functionalized MoS_2 ink, along with the related zeta potential values. **c**, Optical image of a IDE device covered with BDT-functionalized MoS_2 ink *via ex-situ* approach.

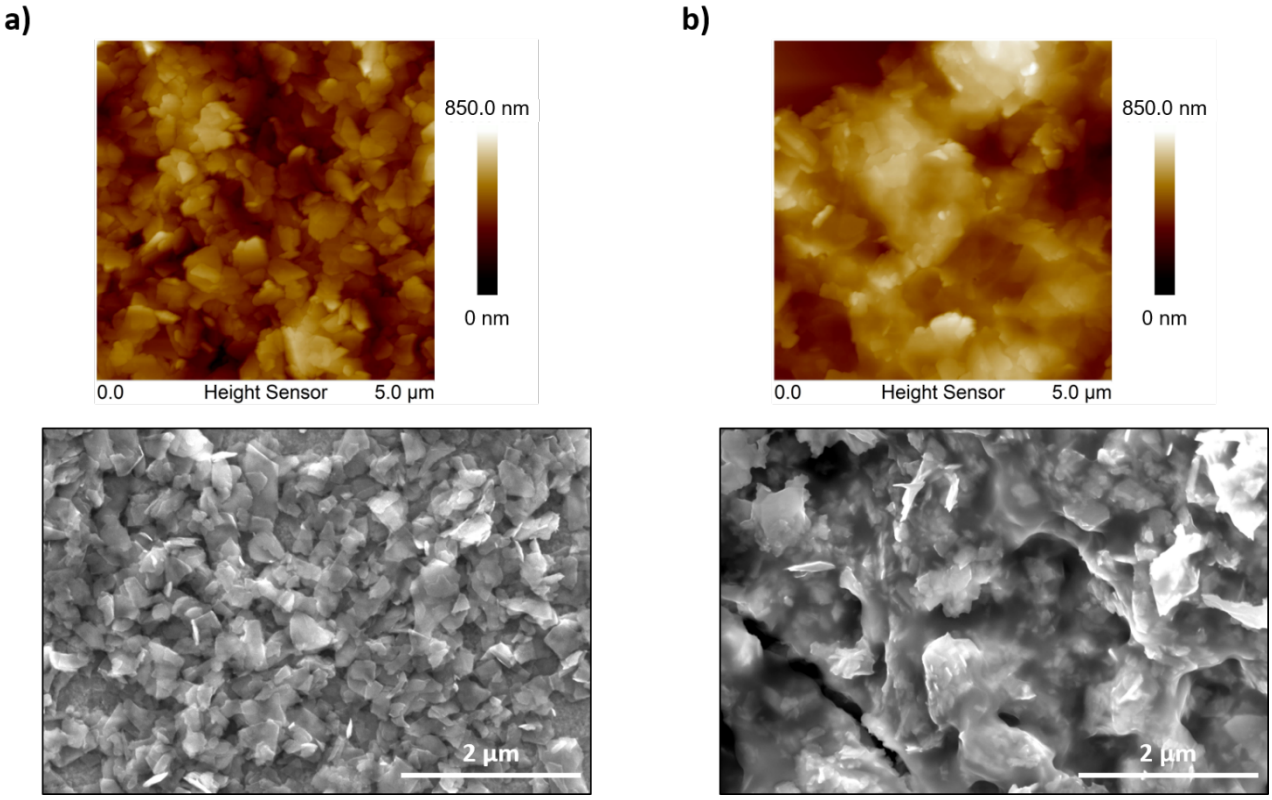
To further study the *ex-situ* reaction of MoS_2 with BDT, we perform dynamic light scattering (DLS) measurements (Supplementary Fig. 29). These results endorse the network formation by BDT molecules. However, the formation of a long-range network only happens when the 2D materials are previously deposited on a surface (*in-situ*), where no precipitation can occur, hampering the flake bridging process.



Supplementary Fig. 29 | DLS analysis. Hydrodynamic radius of MoS_2 flakes dispersed in IPA and functionalized by *ex-situ* approach with BDT molecules. Each sample is prepared by collecting 500 µl of the ink, successively subjected to 1:100 dilution and sonication/mixing steps.

Ex-situ BDT-functionalized MoS_2 films have poor electrical performance, with μ_{FE} one order-of-magnitude lower than pristine MoS_2 films along with identical I_{ON}/I_{OFF}. As reported in Supplementary Fig. 30, AFM and SEM show MoS_2 clusters embedded in an organic matrix, very likely produced by thiol oxidation reactions occurring within the solution exposed to ambient conditions. This prevents an optimal deposition onto IDEs and network formation, giving detrimental effects on electrical performance[28] (Supplementary Table 7).

Static water contact angle measurements on *ex-situ* BDT-functionalized MoS_2 films show a decreased average value, with a consistent shift towards a more hydrophilic behaviour. In particular, *ex-situ* functionalized samples present an average contact angle ~96 ± 2°, different from the 121 ± 2° of *in-situ* samples. From the excellent patternability of the *ex-situ* functional inks towards Au IDEs and all other gathered information, we conclude that the material mainly consists of MoS_2 clusters embedded in a matrix presenting free thiol groups[17].



Supplementary Fig. 30 | Comparison of MS_2 morphological features between *in-situ* and *ex-situ* functionalization approaches. AFM images (top) and SEM images (bottom) taken for MoS_2 films functionalized **a**, *in-situ* and **b**, *ex-situ* with BDT.

Device figure of merit	MoS_2 Film	MoS_2 Clusters (*ex-situ*)	MoS_2 Network (*in-situ*)
μ_{FE} ($cm^2\ V^{-1}\ s^{-1}$)	10^{-3}	10^{-4}	10^{-2}
I_{ON} / I_{OFF}	10^3	10^3	10^4
V_{th} (V)	1.9 ± 0.1	1.8 ± 0.1	1.8 ± 0.1

Supplementary Table 7: Summary of electrical performances for MoS_2 films, networks and clusters, assessed according to the main characteristic device figures of merit: μ_{FE}, I_{ON} / I_{OFF} and threshold voltage (V_{th}), in LG-TFTs.

10. References

1. Paton, K. R. & Coleman, J. N. Relating the optical absorption coefficient of nanosheet dispersions to the intrinsic monolayer absorption. *Carbon* **107**, 733–738 (2016).
2. Backes, C. *et al.* Edge and confinement effects allow in situ measurement of size and thickness of liquid-exfoliated nanosheets. *Nat. Commun.* **5**, 1–10 (2014).
3. Backes, C. *et al.* Production of highly monolayer enriched dispersions of liquid-exfoliated nanosheets by liquid cascade centrifugation. *ACS Nano* **10**, 1589–1601 (2016).
4. Mishra, A. K., Lakshmi, K. V. & Huang, L. Eco-friendly synthesis of metal dichalcogenides nanosheets and their environmental remediation potential driven by visible light. *Sci. Rep.* **5**, 15718 (2015).
5. Rahman, M., Davey, K. & Qiao, S.-Z. Advent of 2D rhenium disulfide (ReS_2): fundamentals to applications. *Adv. Funct. Mater.* **27**, 1606129 (2017).
6. Saito, R., Tatsumi, Y., Huang, S., Ling, X. & Dresselhaus, M. S. Raman spectroscopy of transition metal dichalcogenides. *J. Phys.: Condens. Matter* **28**, 353002 (2016).
7. Lin, Z. *et al.* Defect engineering of two-dimensional transition metal dichalcogenides. *2D Mater.* **3**, 022002 (2016).
8. Zhou, S. *et al.* Atomic structure and dynamics of defects in 2D MoS_2 bilayers. *ACS Omega* **2**, 3315–3324 (2017).
9. Joensen, P., Crozier, E. D., Alberding, N. & Frindt, R. F. A study of single-layer and restacked MoS_2 by X-ray diffraction and X-ray absorption spectroscopy. *J. Phys. C: Solid State Phys.* **20**, 4043–4053 (1987).
10. Donarelli, M., Bisti, F., Perrozzi, F. & Ottaviano, L. Tunable sulfur desorption in exfoliated MoS_2 by means of thermal annealing in ultra-high vacuum. *Chem. Phys. Lett.* **588**, 198–202 (2013).
11. Bouvard, O., Krammer, A. & Schüler, A. In situ core-level and valence-band photoelectron spectroscopy of reactively sputtered tungsten oxide films. *Surf. Interface Anal.* **48**, 660–663 (2016).
12. Borowiec, J. *et al.* Room temperature synthesis of ReS_2 through aqueous perrhenate sulfidation. *J. Phys.: Condens. Matter* **30**, 055702 (2018).
13. Steudel, R. Mechanism for the formation of elemental sulfur from aqueous sulfide in chemical and microbiological desulfurization processes. *Ind. Eng. Chem. Res.* **35**, 1417–1423 (1996).
14. Mignuzzi, S. *et al.* Effect of disorder on Raman scattering of single-layer MoS_2. *Phys. Rev. B* **91**, 195411 (2015).
15. Chakraborty, B. *et al.* Symmetry-dependent phonon renormalization in monolayer MoS_2 transistor. *Phys. Rev. B* **85**, 161403 (2012).

16. Bae, S. *et al.* Defect-induced vibration Modes of Ar^+-Irradiated MoS_2. *Phys. Rev. Appl.* **7**, 024001 (2017).
17. Marques, M. E., Mansur, A. A. P. & Mansur, H. S. Chemical functionalization of surfaces for building three-dimensional engineered biosensors. *Appl. Surf. Sci.* **275**, 347–360 (2013).
18. Chhowalla, M. *et al.* The chemistry of two-dimensional layered transition metal dichalcogenide nanosheets. *Nat. Chem.* **5**, 263–275 (2013).
19. Chen, X. & McDonald, A. R. Functionalization of two-dimensional transition-metal dichalcogenides. *Adv. Mater.* **28**, 5738–5746 (2016).
20. Chen, X., McGlynn, C. & McDonald, A. R. Two-dimensional MoS_2 catalyzed oxidation of organic thiols. *Chem. Mater.* **30**, 6978–6982 (2018).
21. Li, Q. *et al.* Towards a comprehensive understanding of the reaction mechanisms between defective MoS_2 and thiol molecules. *Angew. Chem. Int. Ed.* **56**, 10501–10505 (2017).
22. Förster, A., Gemming, S., Seifert, G. & Tománek, D. Chemical and electronic repair mechanism of defects in MoS_2 monolayers. *ACS Nano* **11**, 9989–9996 (2017).
23. Kelly, A. G. *et al.* All-printed thin-film transistors from networks of liquid-exfoliated nanosheets. *Science* **356**, 69–73 (2017).
24. Shu, J. *et al.* The intrinsic origin of hysteresis in MoS_2 field effect transistors. *Nanoscale* **8**, 3049–3056 (2016).
25. Chiu, F.-C. A review on conduction mechanisms in dielectric films. *Adv. Mater. Sci. Eng.* **2014**, 578168 (2014).
26. Retamal, J. R. D., Periyanagounder, D., Ke, J.-J., Tsai, M.-L. & He, J.-H. Charge carrier injection and transport engineering in two-dimensional transition metal dichalcogenides. *Chem. Sci.* **9**, 7727–7745 (2018).
27. Vladimirov, I. *et al.* Bulk transport and contact limitation of MoS_2 multilayer flake transistors untangled via temperature-dependent transport measurements. *Phys. Status Solidi A* **212**, 2059–2067 (2015).
28. Simonetti, O. & Giraudet, L. Sub-threshold current in organic thin film transistors: influence of the transistor layout. *Org. Electron.* **14**, 909–914 (2013).